

Synthesis and Characterization of Polymer Gel Electrolytes for Supercapacitor

Htein Win¹, Cho Mar Aye²

Faculty of Advanced Materials Engineering^{1,2}

University of Technology (Yatanarpon Cyber City)^{1,2}

Pyin Oo Lwin, Myanmar^{1,2}

kohtlein@gmail.com¹, thazincho.tzc2@gmail.com²

Abstract

The leakage or evaporation of liquid electrolyte is a strong problem that faces in supercapacitor. The development of a supercapacitor that pursue for the advantages of easily carrying, high capacitance and no leaking has been a major objective at the moment. Here gel polymer electrolytes containing PVA and different contents of salt mixture with DMF as solvent were synthesized. Therefore, their effects on the performance of supercapacitors were investigated. The active electrode of the supercapacitors was made from activated carbon. The results indicate that the sodium salt content in gel electrolyte change the performance of supercapacitors. The capacitance, energy density and power density of the highest salt content in electrolyte showed 11.783 Fg⁻¹, 0.00016 Wh/kg and 0.0576 W/kg. This result presented the highest performance of supercapacitor.

Keywords- Supercapacitor, Gel polymer electrolyte, Capacitance, PVA, Complexation

1. Introduction

Supercapacitors with gel electrolytes have recently attracted much research attention in modern technology because they provide many advantages than the original capacitors such as higher charge-discharge, avoiding leaking electrolyte liquid, good mechanical stability [1]. Gel polymer electrolyte (GPE) films composed of a polymer matrix, salt, and plasticizer have received considerable attention owing to their performance, such as high safety, flexibility, and high ionic conductivity. Meanwhile, they are capable of replacing both the liquid electrolyte and separator in batteries or supercapacitors [2]. Additionally, there are many different types of metal salt systems that can be added into polymer to provide higher conductive ionic such as lithium salt (Li₂SO₄, LiCl, LiClO₄, LiBr, LiTFSI), sodium salts (Na₂SO₄, NaClO₄, NaBr, NaI, CH₃COONa).

Poly vinyl alcohol (PVA) is widely used in gel polymer electrolyte for supercapacitors. The main advantages of PVA in gel polymer electrolyte are their ability to solvate large amount of alkali-metal salts, their high ionic conductivities at temperature below the glass temperature, high mechanical strength and reduction of electrolyte leakage risk [1]. PVA is a water-soluble polymer, so its hydrogel can form thin,

uniform films as solid electrolyte for supercapacitors. Furthermore, the high dielectric constant, excellent charge storage capacity and dopant-dependent electrical properties make PVA a promising candidate in the development of supercapacitors.

There are concerns about the cost of lithium if the demands for this technology stretch into larger scale transport and electrochemical device applications. Therefore, to overcome this problem, sodium-based electrolytes have been selected for the present study. The selection of the salt is due to its lower cost, ready availability, lower toxicity and low atomic mass. The sodium-based electrolyte system possessed higher ionic conductivity at room temperature [3].

The main advantage of using sodium metal ion is its availability in abundance at a cheaper cost than lithium. Further, more softness of the material makes it easier to achieve good contact with other components in the battery. In the present investigations, an attempt has been made to characterize polymer electrolytes based on PVA complexed with sodium iodide (NaI) salt at different weight percentages to evaluate its potential in electrochemical cells [4].

Nature of salt, size of cation and anion, salt's lattice energy, organic/ inorganic salt etc, plays very important role in polymer electrolyte's behavior determination. It has been found that larger anion results in amorphous matrix and provides path for cation movement hence a large conductivity is found in these system [5].

The most important advances in increasing the ionic conductivity of polymer electrolytes were brought into effect by the incorporation of suitable amounts of plasticizers. Because plasticizers are low in molecular weight, nonvolatile substances (mostly liquids) that, when added to a polymer, improve its flexibility, processability, and, hence utility. Generally, low molecular weight, high dielectric constant polar organic solvents such as ethylene carbonate (EC), propylene carbonate (PC), polyethylene glycol (PEG), dimethylformamide (DMF), dimethylsulfoxide (DMSO), diethyl phthalate (DOP) and dibutyl phthalate (DBP) have been used in polymer electrolytes to enhance their room temperature ionic conductivities. The conductivities of these electrolytes critically depend on the physical properties of the plasticizer such as its viscosity and dielectric constant. A plasticizer improves the electrical conductivity of polymer electrolyte by (i) increasing the amorphous content of polymer electrolytes; (ii) dissociating ion aggregates present in polymer electrolytes and (iii) lowering the

glass transition temperature. DMF is used as a (solvent) plasticizer for NaI doped PVA.

Supercapacitors with the gel polymer electrolyte containing polyvinyl alcohol (PVA) as polymer, sodium iodide as salt and dimethyl formamide (DMF) as solvent were fabricated and investigated. Then, the electrochemical properties of supercapacitors were studied by using two electrodes testing cell to determine their performance [6].

Complexation: A coordination complex is the product of a Lewis acid-base reaction in which neutral molecules or anions (called ligands) bond to a central metal atom (or ion) by coordinate covalent bonds. Complexation of a ligand with a substrate molecule can occur as a result of coordinate covalent bonding or one or more of the following noncovalent interactions: Van der Waals forces, Dipolar forces, Electrostatic forces, Hydrogen bonding, Charge transfer, Hydrophobic interactions. Complexation of Polymer-metal is electrostatic attraction. Complexation of iodine with polyvinyl alcohol to improve aqueous solubility of active agent [7].

2. Literature Review

Gel electrolytes are a new class of electrolytes being used for making flexible supercapacitors. A gel electrolyte is a mixture of polymer, salt and the solvent. This can be formed by mixing organic liquid solvent with a salt and then polymer is added to give mechanical stability, which results in formation of gel. Various polymers such as polyvinyl alcohol (PVA), vinylidene fluoride (PVDF) and poly (vinylidene fluoride-co-hexafluoropropylene) (P (VDFHFP)) have been used for making gel electrolytes. PVA/H₃PO₄ and PVA/H₂SO₄ gel electrolyte are the mostly used gel electrolytes for making supercapacitors.

By using gel electrolyte, it has the advantage of being safe and flexible without the need of any separator. Flexible supercapacitors are prepared by graphene-based electrodes with gel electrolytes. It is reported that acidic based gel electrolyte PVA/H₂SO₄ shows higher capacitance values than alkaline gel electrolytes PVA/KCl and PVA/NaCl. After comparing the specific capacitance values of flexible supercapacitors made with six difference gel electrolytes PVA/KCl, PVA/NaOH, PVA/NaCl, PVA/KOH, PVA/H₂SO₄, PVA/H₃PO₄ it has been reported that PVA/H₂SO₄ gives maximum specific capacitance of 820 μF/cm² and PVA/NaCl gives minimum capacitance of 0.5 μF/cm² [8].

Commercially, supercapacitors based on carbon materials are in high demand owing to their properties like being semi-permanent, ecofriendly, and having high-power density compared to the batteries. Recently much research has been devoted to improving the energy density of the supercapacitor, so it is gradually replacing the battery in the field of energy storage systems.

The SCs based on liquid electrolyte consist of a solid frame with positive/negative electrodes and separator which is filled with liquid electrolytes. These SCs have

various practical difficulties due to lack of physical flexibility, so it is hard to be applied to various shapes of electronic devices, and the sturdy exterior surrounding material increases the weight of devices. Moreover, the exterior structure if damaged could result in electrolyte leakage that can cause corrosion of the device. To overcome these difficulties, research on polymer electrolytes has been widely encouraged; since polymer electrolytes can reduce the risk of leakage due to their quasi-solid-state form and also afford promising properties like flexibility, elasticity, high ionic conductivity, chemical/ electrochemical stability and affinity with the electrodes [9].

3. Experimental Procedure

3.1. Materials

We have chosen N,N-dimethyl-formamide as the solvent i.e. (CH₃)₂NC(O)H. It has –O group which participates in the formation of the coordinate bond. It has a higher dielectric constant that helps in the dissolution of salt.

Salt (NaI): The anionic part of the salt that we have chosen is bulky as compared to the cationic part. So the cationic part i.e. Na⁺ comes out easily and thus provides ions for conduction. The salt possesses low lattice energy too.

Poly(vinyl alcohol) (PVA) (C₄H₆O₂)n is an water-soluble synthetic polymer and possesses the capability to form hydrogels by chemical or physical methods.

Poly (vinyl alcohol) (PVA) with an average molecular weight of 14,000 g/mol, dimethyl formamide (DMF), sodium iodide (NaI) were utilized for preparation of polymer gel electrolytes. These raw materials are locally available. Moreover, activated carbon, aluminum foil, binder (glue) and distilled water were also the requirements for fabricating of supercapacitors.

3.2. Synthesis of Polymer Gel Electrolytes

Gel polymer electrolyte was prepared by mixing 20 ml of dimethyl formamide and 2g of PVA with different weight of sodium iodide salts. Here, the different weights of sodium iodide were 1.94 g, 0.65 g and 0.39 g respectively. The solution of mixture was heated at 100°C and stirred about 2h to obtain homogeneous solution. After heating and stirring, the total salt-solvent-polymer solution was casted onto petridish and left for few days for gelation process. The same preparation was followed to synthesize different gel electrolytes by keeping the amount of PVA constant and by varying the concentration of salt. The preparation of gel electrolyte was shown in Figure 1.

3.3. Fabrication of Activated Carbon Electrodes and Supercapacitor



Figure 1. Preparation of Gel Electrolyte at 100 °C by Magnetic Stirrer



Figure 2. Electrodes

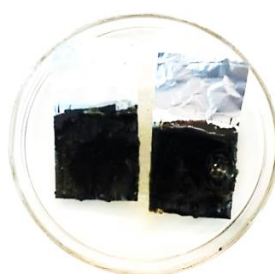


Figure 3. Electrodes after Dipping in Electrolyte

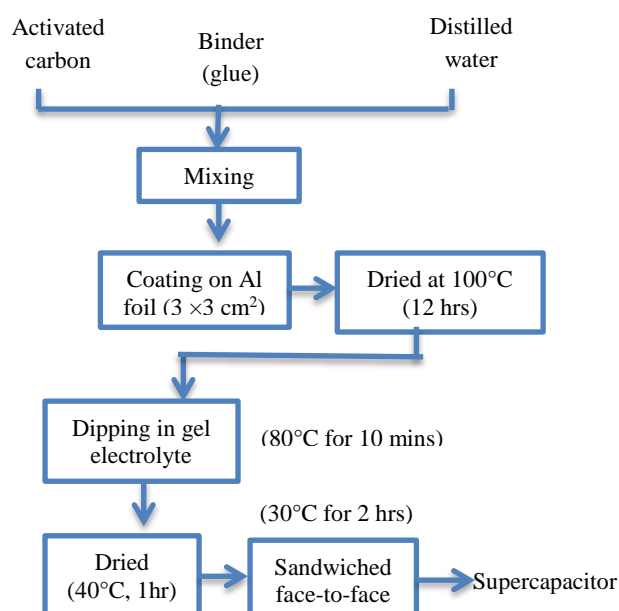


Figure 4. Flow Chart for Preparation of Supercapacitor

For preparation of electrode, the activated carbon was first grinding by using ball-mill for making powdered activated carbon. The activated carbon of about 50 g has run for one hour at 200 rpm and the resulting size of activated carbon was about ten microns in diameter. The electrodes were fabricated by mixing 80 wt. % of activated carbon (AC), 20 wt. % of binder (glue) with distilled water. Then, the obtained viscous paste was coated on aluminum foil ($3 \times 3 \text{ cm}^2$) and dried at 100°C in vacuum oven for 12 hours. The photographic image of as fabricated electrodes is shown in Figure 2.

The overall flow chart for assembling of supercapacitor is shown in Figure (4).

For a supercapacitor fabrication, two activated carbon electrodes were dipped in the PVA gel electrolyte for 10 minutes at 80 °C and dried on the hot plate at 40 °C for one hour. The electrodes after dipping in gel electrolyte can be seen in Figure 3. After drying excess solvent in the electrolyte, the electrodes were sandwiched face-to-face and sealed using vacuum tape to form a full cell. Finally, this supercapacitor was dried at 30 °C in a vacuum oven for two hours.

3.4. Characterizations

IR spectrums for these prepared samples were performed by using spectrum 400 FTIR (Perkinelmer) Spectrophotometer to express the complexation process in the polymer gel electrolytes. The measurements were taken over a range of 400-4,000 cm^{-1} wavenumber. The electrochemical experiments were performed in full cell configuration for the entire gel polymer electrolyte-based supercapacitors.

The specific capacitance (C_{cell} , F/g) of testing cell was calculated via the following equation (5):

$$C_{\text{cell}} = \frac{I \times \Delta t}{m \times \Delta V} \quad (1)$$

Where I (A) is the discharge current, Δt (s) is the discharging time, m (g) is the total mass of active material on electrode and ΔV is the discharge voltage after V_{drop} .

The energy density (E , Wh/kg) and power density (P , W/kg) can be also calculated by the following formula [6, 7]:

$$E = \frac{1}{2} \times \Delta V^2 \times C \times \frac{1000}{3600} \quad (2)$$

$$P = \frac{E}{\Delta t} \times 3600 \quad (3)$$

By following the above equations, the capacitance, energy density and power density of the supercapacitors can be calculated.

4. Results and Discussion

4.1. Fourier Transform Infrared (FTIR) Analysis

The present of various functional groups of PVA/NaI electrolytes were analyzed using FTIR

spectra. Figure (5) shows the FTIR spectra of PVA based electrolytes with different concentrations of NaI contents. The wide absorption bands between 3,650-3,200 cm⁻¹ is representing the stretching vibration of O-H of the intermolecular and intermolecular hydrogen bonds. These regions show the present of an alcohol group. Alcohols have a very distinct strong and broad shape. In addition to this, the band around 2,960-2,850 cm⁻¹ corresponds to the stretching band of C-H from alkyl groups. The band around 1437 cm⁻¹ belongs to O-H bending vibration for all concentration NaI. Moreover, the resultant spectrum between 1850-1650cm⁻¹ wavenumber show the stretching of the C=O groups. The C-O stretching is observed at 1101, 1099 and 1091 cm⁻¹ for different composition of salts and the spectra show slight shift in the peak positions.

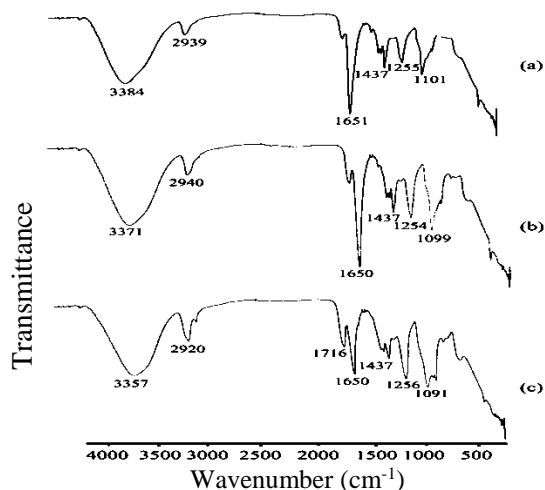


Figure 5. FT-IR Spectra of PVA Gel Electrolyte with Different Concentration of (a) O/Na =20, (b) O/Na =60 and (c) O/Na =100

The bands occurring at 1255, 1254 and 1256 cm⁻¹ wavenumbers correspond to the C-C stretching. All these changes in the FTIR spectra are clear indication for the complexation of PVA with NaI salt.

4.2. Electrochemical Properties of Supercapacitors

The charging characteristics of supercapacitors with different gel electrolytes show in Figure 6. The fabricated supercapacitor with the highest salt content in electrolyte is named as sample 1, the middle content of salt as sample 2 and the less content of salt in electrolyte is sample 3.

The voltage was measured for every 10 s of charging state for various samples. The initial state of charging sample 1 show 0.71 V at 10 s of charging, sample 2 and 3 are 0.64 V and 0.43 V respectively. After charging of about 30 s, the voltage rise to 1.16 V for sample 1 and it is about 0.45 V increased after charging 20 s. For sample 2 and 3, the voltages reach to 0.95 V and 0.85 V. The increase voltages are 0.31V

and 0.42 V for these two samples. After 50s charging, the voltages are 1.18V, 1.17 V and 1.07 V and these voltages remain the same after 60 s charging. Therefore, it can be said that all samples are needed about 60 s for fully charging. The increased in voltage is not time dependable and it is depending on the number of ion mobile in electrolytes. So, the voltage increase in every 10 s may not be the same.

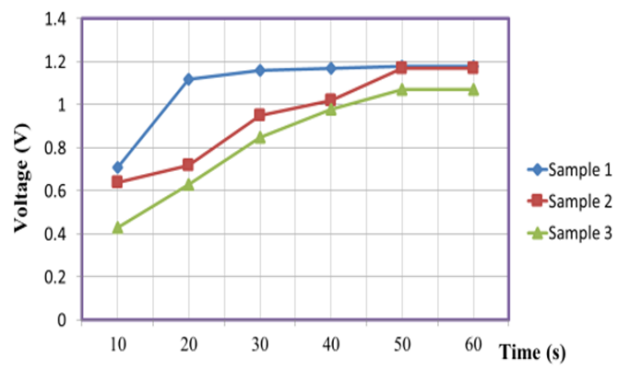


Figure 6. Comparison of Charging Characteristics for Three Samples

To test the self-discharge rate of the sample produced, the stored voltage of the sample is measured day by day. On 2nd day, the voltage dropped from 1.24 V to 1.18 V for samples 1. On the next day, the voltage decreased to 0.6 V. After about one week, the sample loss its voltages to 0.17 V. For sample 2, the voltage dropped to 0.42 V from 1.17 V after two days and about 0.09 V was lost after the one week. After one week last, almost all voltages in samples 3 decreased. Experiments show a dependency of the self-discharge duration and short-term history. Self-discharging in experiment caused due to cell overvoltage and current leakage between two electrodes.

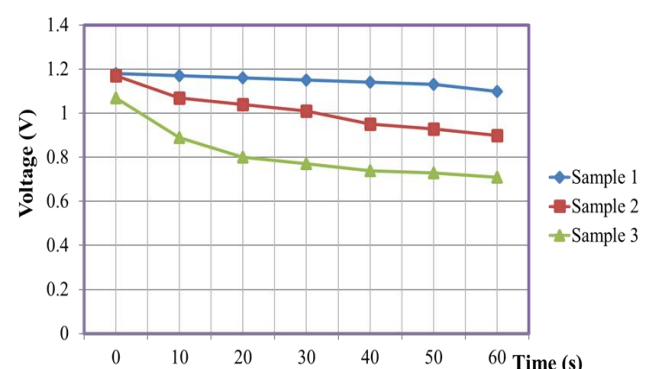


Figure 7. Comparison of Discharging Characteristics for Three Samples

The discharge characteristics of different samples are described in Figure 7. As shown in Figure, the voltage of sample 1 drops from 1.18 V to 1.17 V after discharge about 10 s. After 30s, the voltage decreases to 1.15 V and the voltage reach about 1.1 V after 60 s discharge. It can be seen that only 0.08 V is lost after 60 s. In sample 1, the voltage drops steadily about 0.01

V for every 10s measurement except for the voltage drop from 50 s to 60s. In this way, after an hour, this sample will be fully discharged. For sample 2, the voltage decreases from 1.17V to 1.07 V after 10 s and about 0.1 V is lost during this time. The voltage reduces to 1.01 V after 30 s and 0.9 V after 60s. The voltage about 0.27 lost during 60 s and the voltage drop is not quite steady if compare to sample 1. From sample 3, after discharging 10 s the voltage reduces from 1.07 V to 0.89 V. The voltage drops to 0.77 V after 30 s and 0.71 V after 60 s. About 0.36 V lost during one minute and the voltage drop is not also steady state. The voltage drop is independent of time and the voltage reduced rate cannot be the same for every 10 s discharging state. However, the voltage drops in sample 1 shows the steadiest condition.

The improvement of electrochemical properties of the gel electrolytes are clearly observed in Table 1. As described in table, the performance of supercapacitors is increased with increasing of sodium salt content in the gel polymer electrolyte. The supercapacitor with the highest content of sodium salt mixture in gel electrolyte shows the greatest specific capacitance, energy density and power density.

Therefore, this result indicates that the ions transfer in gel polymer electrolytes are significantly improved at high content of sodium salt mixture. Thus, it can also be concluded that sample 1 with highest amount of salt presents the greatest performance of supercapacitor.

Table 1. Specific Capacitance, Energy Density and Power Density of Supercapacitors

Performance	Sample 1	Sample 1	Sample 1
C cell (F/g)	11.783	0.62381	0.5739
E (Wh/kg)	0.00016	0.00008	0.00007
P (W/kg)	0.0576	0.02714	0.02592

5. Conclusion

Gel polymer electrolytes based on PVA/NaI have been utilized for fabrication of activated carbon supercapacitor. Supercapacitors were assembled with different gel electrolyte compositions and their electrochemical properties were investigated. The performance of supercapacitors was improved by increasing of NaI salt mixture content in the polymer gel electrolytes. At the highest amount of sodium salt, the maximum specific capacitance value of 11.783 F/g, high energy density and power density of 0.00016 Wh/Kg and 0.0576 W/kg, respectively were obtained. This result also suggested that fast ion transport take place in highest amount of sodium salt content in polymer gel electrolyte. Therefore, the results obtained in this work confirm that the gel polymer electrolytes are interesting development for replacing liquid electrolytes in supercapacitors.

6. References

- [1] Boschin A, Johansson P, "Characterization of NaX (X: TFSI, FSI) – PEO based solid polymer electrolytes for sodium batteries", vol-175, p 124-133, 2015.
- [2] J. Wang, Z. Zhao, S. Song , Q. Ma and R. Liu: "High Performance Poly (vinyl alcohol)-Based Li-Ion Conducting Gel Polymer Electrolyte Films for Electric Double-Layer Capacitors", *Polymers*, vol-10, 1179, 2018.
- [3] Nurul Akmaliah Dzulkurnain, Azizan Ahmad, "P(MMA-EMA) Random Copolymer Electrolytes Incorporating Sodium Iodide for Potential Application in a Dye-Sensitized Solar Cell", *Polymers*, vol-7, 266-280, 2015.
- [4] P. Balaji Bhargav, V. Madhu Mohan, A. K. Sharma, "Structural and electrical studies of sodium iodide doped poly (vinyl alcohol) polymer electrolyte films for their application in electrochemical cells", *Ionics*, 13:173-178, 2007.
- [5] Neelam Srivastava, Tuhina Tiwari, "New trends in polymer electrolytes: a review", *e-Polymers*, no.146, 2009.
- [6] P. Chandra Sekhar, P. Naveen Kumar, "Effect of plasticizer on conductivity and cell parameters of (PMMA+NaClO₄) polymer electrolyte system", *Journal of Applied Physics*, vol-2, 4, p-1-6, 2012.
- [7] Arshad Khan, "Introduction, Classification of Complexation, Applications, methods of analysis", Raghavendra Institute of Pharmaceutical Education and Research (RIPER), 2018.
- [8] L.L. Zhang, Rui Zhou, X.S Zhao, "Graphene- based materials as supercapacitor electrodes", *Journal of Materials Chemistry*, 20, 5983, 2010.
- [9] Jang, H., Raj, C. Justin., Lee, Kim, "Enhanced supercapacitive performances of functionalized activated carbon in novel gel polymer electrolytes with ionic liquid redox-mediated poly (vinyl alcohol)/phosphoric acid", *Royal Society of Chemistry*, 6 (79), 75376-75383, 2016.
- [10] Xing Z, Liang Liang W, Jing P, "A Flexible Ionic Liquid Gelled PVA-Li₂SO₄ Polymer Electrolyte for Semi-Solid-State Super capacitors", *Advanced Materials Interface*, October 19, 2015.
- [11] Meng C, Liu C, Chen L, Hu C and Fan S, "Highly Flexible and All-Solid-State Paper like Polymer Supercapacitors", *Nano Letter*, vol-10, p 4025, 2010.
- [12] Boschin A, Johansson P, "Characterization of NaX (X: TFSI, FSI) – PEO based solid polymer electrolytes for sodium batteries", vol-175, p 124-133, 2015.

Effect of the Additives on Electrical Properties of Zinc Oxide Varistor by Powder Metallurgy Method

Saw Mya Ni ¹, Myo Theint Theint Tun ²

Faculty of Advanced Materials Engineering^{1,2}

University of Technology (Yatanarpon Cyber City)^{1,2}

Pyin Oo Lwin, Myanmar^{1,2}

sawmyani2017@gmail.com¹, myotheint.mtth11@gmail.com²

Abstract

Zinc oxide varistors are largely used to protect the electric and electronic circuits and components against overvoltage. This paper describes the electrical properties of zinc oxide varistor produced by powder metallurgy method. Zinc oxide varistors based on Bi_2O_3 , Sb_2O_3 , MnO and Co_2O_3 were prepared by the powder metallurgy method. The raw material powders were mixed using mixer. After mixing the powders, cylindrical shaped samples were pressed and sintered for 1 hour at temperatures in 1000°C. The sintered samples were characterized by X-ray fluorescence, X-ray diffraction analysis and Scanning Electron Microscopy for phase identification. Electrical properties; current-voltage characterization and non-linear coefficient were also measured to characterize the properties of zinc oxide varistor.

Keywords- Powder Metallurgy, Zinc Oxide, Electrical Properties, Additive Oxides

1. Introduction

Varistors or variable resistors are sintered polycrystalline ceramic and have been used as a surge protective device for decades. The main reason is their nonlinear current-voltage (I-V) characteristics and good energy absorption capability. Zinc oxide (ZnO) varistors were first used for the purpose of protection of semiconductor devices against transient surges in TV sets, microwave ovens, and other consumer electronic equipment. Later, ZnO varistors were extensively used as surge absorbers in industrial electronic equipment, and the fields of application have risen regularly. ZnO varistors have become one of the most useful protection devices and are very important devices in transient surge suppression technology. ZnO varistors are applicable as characteristics elements in gapless-type lightning arresters used in electric power systems. Moreover, automotive use

has also been by the improvements of the characteristics for high operating temperature and low operating voltages [1].

At low voltage, varistors act as resistors, however they become conductors at high voltage. In normal situations, a small current is passed from the power supply. However, there may be a large current in abnormal situations and varistor draws the current to ground. In the past, ceramics used as varistors were made of silicon carbide (SiC) [2]. Zinc oxide has largely replaced silicon carbide-materials because of their superior high nonlinear behavior, providing improved circuit protection. ZnO varistors consist of ZnO as the major ingredient and several kinds of additives. The additives such as Bi_2O_3 , MnO_2 , Cr_2O_3 , and etc. can generate the nonohmic property and improve the electrical properties and the stability. A typical varistor formation could be from 96.5mol% ZnO, 0.5mol% Bi_2O_3 , 1 mol% Co_2O_3 , 0.5 mol% MnO , 1 mol% Sb_2O_3 , and 0.5 mol% Cr_2O_3 [3]. Amongst these additives, Bi_2O_3 plays the most important role and segregates to the grain boundary interface [4].

2. Theoretical Background

A varistor is a voltage dependent resistor (VDR). The resistance of a varistor is variable and depends on the voltage applied. The word "varistor" is composed of parts of the words "variable resistor". Their resistance decreases when the voltage increases. In case of excessive voltage increases, their resistance drops dramatically. This behavior makes them suitable to protect circuits during voltage surges. Causes of a surge can include lightning strikes and electrostatic discharges. The most common type of VDR is the metal oxide varistor or MOV [5].

The electrical properties of ZnO varistors mostly include the current voltage characteristics, the capacitance-voltage characteristics and the breakdown voltage/field, and the effect of additives oxides on its properties. However, the current-voltage characteristics

are the most important property of a ZnO varistor. The varistor functionally behaves as a near insulator (resistor) prior to reaching a voltage known as the breakdown or threshold voltage and it behaves as a conductor thereafter. The attractive features of the ZnO varistor are the nonlinear or nonohmic characteristic in the conductive mode. The I-V characteristics of ZnO varistors include three regions i.e. the pre-breakdown region, the nonlinear region, and the upturn region. The current-voltage relation can be expressed in a term of

$$I = kV^\alpha \quad (1)$$

where k is a constant, and α is nonlinear coefficient.

Therefore, a nonlinear coefficient is defined by

$$\alpha = \frac{\log(I_2/I_1)}{\log(V_2/V_1)} \quad (2)$$

where, V_1 and V_2 are the voltage at current I_1 and I_2 ($I_2 > I_1$), respectively.

Since the invention of ZnO varistors, most of the developments and investigations have been based on the ZnO-Bi₂O₃ system because of its simplicity and efficiency. However, the nonlinearity of the ZnO-Bi₂O₃ binary system did not show the most effective results as the nonlinear coefficient was less than 10 [4]. It means that additives play an important role for ZnO varistors because they can improve the nonlinearity. Metal oxide additives affect various properties of ZnO varistors [6].

2.1. Roles of Additives in Zinc Oxide Varistors

The addition of antimony retards the grain growths. Antimony forms the spinel phase and a pyrochlore phase blocking grain growth. Moreover, Sb promotes the formation of twins in ZnO grains and improves the nonlinearity. Thus, the I-V characteristics become better stabilized against electrical stresses, and the breakdown voltage increases. The roles of Sb₂O₃ were proposed as: (i) grain growth suppression and (ii) the solubility enhancement of ions such as Zn in the Bi₂O₃-rich liquid phase [6]. The latter role is very important in order to control the defect distribution at the grain boundaries during the cooling. To improve the reliability, NiO, Cr₂O₃, or a small amount of glass frit are used. These additives stabilize the intergranular layer against the electric load and ambient conditions e.g. temperature and humidity. Cobalt and manganese are the improvement of nonlinear characteristics. Bismuth is the isolation among ZnO grains and supplying required elements to grain boundaries [7].

3. Experimental Procedure

The experimental procedure of zinc oxide varistor is shown with the schematic flow diagram as follows:

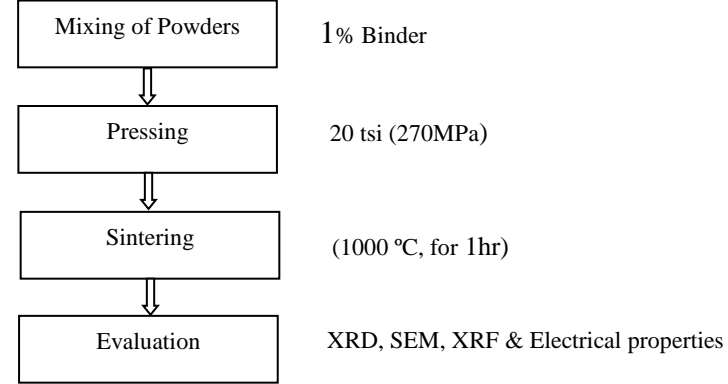
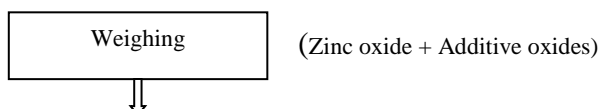


Figure 1. Flow Diagram of Experimental Procedure

Table 1. shows the process variable data in composition. Sample-1 (S₁) is the base composition, Sample-2 (S₂) is the base composition without MnO, Sample-3 (S₃) is the base composition without Co₂O₃ and Sample-4 (S₄) is the base composition without Sb₂O₃. In this research, the main variables are compositions and sintering temperatures.

Table 1. Sample Compositions

Sample	Composition (mol% of metal)				
	ZnO	Bi ₂ O ₃	MnO	Sb ₂ O ₃	Co ₂ O ₃
S ₁	97.0	1.0	0.5	1.0	0.5
S ₂	97.5	1.0	-	1.0	0.5
S ₃	97.5	1.0	0.5	1.0	-
S ₄	98.0	1.0	0.5	-	0.5

3.1. Raw Materials

The main raw material is pure zinc oxide (ZnO) powder. The required additive oxides are bismuth oxide (Bi₂O₃), antimony oxide (Sb₂O₃), manganese oxide (MnO), cobalt oxide (Co₂O₃). All starting materials were purchased locally and they were of reagent grade. The other needed raw materials are binder (polyvinyl alcohol) using in powder mixing and copper electrodes used in electroding step, aluminum foil, gloves.

3.2. Production of ZnO Varistor

In the mixing of the raw material powders, firstly, ZnO powder and additive oxide powder with their respective ratio (shown in Table 1) were blended homogeneously with binder. Polyvinyl alcohol (PVA) was used as binding agent or lubricant to bind the raw material powders and to be sticky each other. The weight of each sample is 20 grams (g). Ceramic ball mill was used to blend the powders homogeneously. It took about 15 minutes for one operation for blending. After mixing, the mixed powders for each sample were compacted at the pressure of 270 MPa

using the hydraulic pressing machine. They were pressed in the cylindrical shaped die made of steel. After five minutes, pressure was removed. The diameter and height of the samples were 25mm and 12mm respectively. In this research, muffle furnace is used for sintering. The green compact samples were heated in the sintering furnace at temperature 1000 °C, for 1hr. Finally, the samples were furnace cooling. To check the composition of the resultant sintered samples, the sample was characterized by X-ray fluorescence imaging (XRF), X-ray Diffraction (XRD), Scanning Electron Microscopy (SEM).

To measure the electrical properties, the sintered samples and the copper electrodes were soldering with electric gun. Once the soldering process had been completed, it was covered by using glue gun like the epoxy coating. After electroding, electrical properties (current-voltage characterization and non-linear coefficient) were also measured.

4. Results and Discussion

4.1. Analysis of Energy Dispersive X-Ray Fluorescence

The EDXRF analysis shows the composition of ingredients contained in the sintered samples as in Table 2. Based on these analyses, the accuracy of the results in all samples is good for all species analyzed. In Table 2, the compositions were changed due to the melting of difference temperature. Partial Bi_2O_3 and Sb_2O_3 volatilization occurs at the temperature of above their melting points. Some impurities (Lu_2O_3 , CuO , Nd_2O_3 , Cr_2O_3) also occur in all samples but they will not affect varistor properties due to low content presents.

Table 2. XRF Analysis of Sintered Samples

Analyte	Result of S ₁	Result of S ₂	Result of S ₃	Result of S ₄
ZnO	97.735 %	97.666%	97.327%	97.801 %
Bi_2O_3	0.762 %	0.746%	1.010%	0.835 %
MnO	0.521 %	×	0.502%	0.495 %
Sb_2O_3	0.512 %	0.815%	1.041%	×
Co_2O_3	0.153 %	0.416%	×	0.321 %
Lu_2O_3	0.118 %	0.113%	-	0.186 %
CuO	0.092 %	0.077%	0.095%	0.079 %
Nd_2O_3	0.069 %	0.089%	-	0.087 %
Cr_2O_3	0.038 %	0.052%	0.025%	0.42

4.2. X-Ray Diffraction Analysis

In XRD patterns of both sample-1 (Figure. 2) and sample-2 (Figure. 3), large peaks of ZnO can be seen and species related to the additives do not appear because of their low content. XRD analysis shows the strong and sharp diffraction peaks as in Figure. 2 and 3. These peaks suggest that the particles were well crystalline.

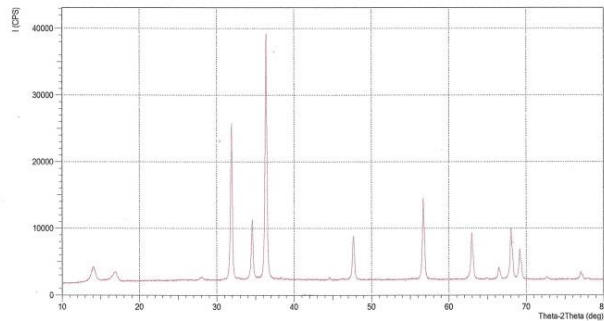


Figure 2. XRD Analysis of Sintered Sample-1

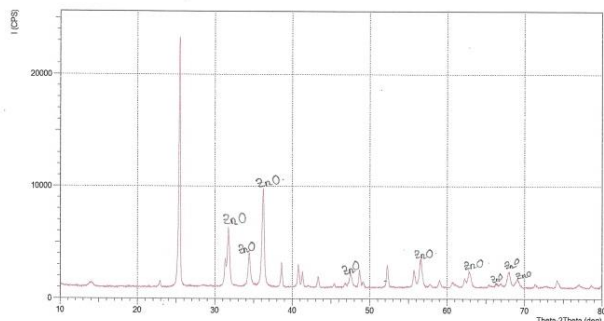
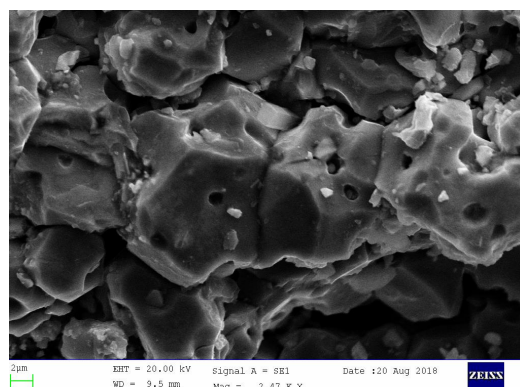
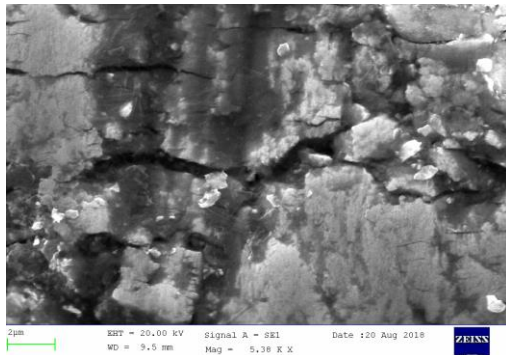


Figure 3. XRD Analysis of Sintered Sample-2

4.3. Scanning Electron Microscopy Analysis



(a)



(b)

Figure 4. SEM Images of (a) Sample-1 and (b) Sample-2 Sintered at Temperature 1000°C for 1hr

The SEM images of sample-1 and sample-2 are shown in Figure. 4 (a) and (b), respectively. In SEM image of sample-1, it can be seen three phases: conductive bulk ZnO grains, continuous resistivity Bi-rich intergranular phase and spinel phase. The fraction of spinel phase in sample-2 is smaller than in sample-1 (Figure. 4(a)), and the size of the grains in sample-1 is smaller than that of sample-2 because antimony retards grain growth.

4.4. Electrical Properties

The comparison of I-V characteristics for four samples is shown in Figure. 5. It can be seen that sample-1 exhibits the highest current whilst sample-4 has the lowest current. As shown in Figure. 6, the absence of MnO or Co₂O₃ causes the reduction of the nonlinear coefficient of these compositions whilst the absence of Sb₂O₃ improves the nonlinear coefficient. The nonlinearity of sample 1 (base composition) has the highest value.

The smaller α -values exhibited by the sample-3 are related to the I-V characteristics. In the range used for determination of the α -value, the flatness of the I-V curve of the sample-3 is less than that of others composition so it will be characterized by poorer electrical properties. Since the presence of cobalt and manganese improves the nonlinearity according to the literature, therefore the nonlinearity of sample-3 (absence of cobalt) and sample-2 (absence of manganese) lead to reduction. Typically, the improvement of non-ohmic exponent of addition of antimony reduces more than that of cobalt and manganese (Co, Mn > Sb) and so the absence of antimony (sample-4) result in the higher nonlinearity.

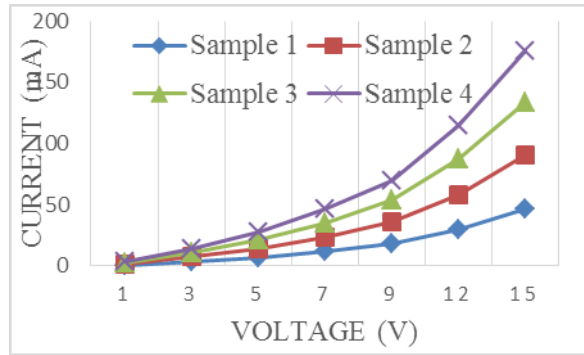


Figure 5. Comparison of Current- Voltage (I-V) Characteristics of Samples at 1000 °C

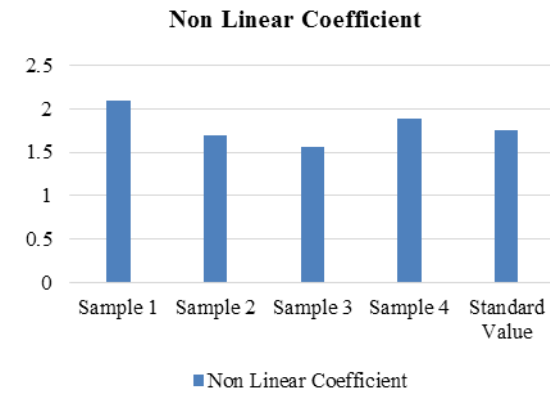


Figure 6. Graph of Non-Linear Coefficient of Samples at Temperature 1000°C

4.5. Comparison of Standard Value and Resulted Value

Table 3. Non Linear Coefficient

Samples	Non linear coefficient (α)
Standard value	1.7600
S ₁	2.0954
S ₂	1.7502
S ₃	1.5665
S ₄	1.8799

Table 3. shows that the non-linear coefficient values of standard zinc oxide varistor have the range between 1 and 53. The resulted values were also in that range. So the samples in this study are said to be non-linear.

5. Conclusion

ZnO based varistors were prepared by the powder metallurgy method. The obtained samples were characterized by XRF analysis, X-ray diffraction analysis, scanning electron microscopy and electrical properties. The samples were made selective removal of different additive oxides. In nonlinear current-voltage characteristics with nonlinear coefficient, four samples at 1000°C were measured and compared. They all exhibited nonlinear current-voltage characteristics, with nonlinear coefficients. According to all results on the effect of additives removal, antimony oxide has more influence than cobalt oxide and manganese oxide on the properties of ZnO varistor.

6. References

- [1] P.R. Bueno, J.A. Varela, E. Longo "SnO₂, ZnO and Related Polycrystalline Compound Semiconductors: An Overview and Review on the Voltage-Dependent Resistance (Non-Ohmic) Feature" Journal of the European Ceramic Society 28 [3] 505-529 (2008)
- [2] A.J. Moulson, J.M. Herbert. "Electroceramics: Materials, Properties, Application" p.130-139 (1997)
- [3] F.D. Martzloff, L.M. Levinson. "Surge-Protective Devices" in L.M. Levinson, editor. 'Electronic Ceramics: Properties, Devices, and Applications' p. 275-305 (1988)
- [4] J. Wong, P. Rao, E.F. Koch "Nature of an Intergranular Thin-Film Phase in a highly Non-Ohmic Metal-Oxide Varistor" Journal of Applied Physics 46 [4] 1827-1830 (1975)
- [5] Protection of Electronic Circuits from Overvoltages, Ronald B. Standler (Dover Books)
- [6] T.K. Gupta. "Ceramics and Glasses" in S.J. Schneider Jr., editor. 'Engineering Materials Handbook' p. 1150-1155 (1991)
- [7] T.K. Gupta. "Microstructural Engineering through Donor Acceptor Doping in the Grain and Grain- Boundaries of a Polycrystalline Semiconducting Ceramic" Journal of Materials Research 7 [12] 3280-3295 (1992)

Effect of CuO-doping on the Structure and Optical Properties of CuO-doped TiO₂ Nanoparticles

Thida San Nwe¹, Matthanakhangkhamano², Lek Sikong³, Kalayanee Kooptarmond⁴

Department of Mining and Materials Engineering^{2,3,4},

Faculty of Advanced Materials Engineering¹, Faculty of Engineering^{2,3,4}

University of Technology (Yatanarpon Cyber City)¹, Prince of Songkla University^{2,3,4}

Pyin Oo Lwin 05087, Myanmar¹, Hat Yai, Songkhla, 90112, Thailand^{2,3,4}

thidasannwe@gmail.com¹, kmatthan@eng.psu.ac.th², lek.s@psu.ac.th³, kalayaneek@psu.ac.th⁴

Abstract

CuO-doped TiO₂ nanoparticles were synthesized by using sol-gel method to investigate the structural and optical properties on the CuO doping. The crystal structure, morphology and optical properties of pure TiO₂ and CuO-doped TiO₂ nanoparticles were examined by X-ray diffraction (XRD), scanning electron microscope (SEM) and UV-Vis spectrophotometer, respectively. In the case of CuO doping, the spherical and clew-like structure of CuO-doped TiO₂ nanoparticles densely occurred at 10 mol% CuO. The CuO-doped TiO₂ nanoparticles exhibited the absorption edge with a longer wavelength and narrow band gap energy of the optical properties.

Keywords- CuO-doped TiO₂ nanoparticles, Structural properties, Optical properties, Sol-gel method

1. Introduction

Recently, research has been conducted new semiconductor with better properties to modify properties of titanium dioxide (TiO₂). In general, TiO₂ is a wide-band-gap semiconductor and displays short wavelength less than 400 nm under UV light [1]. Therefore, TiO₂ was designed by doping metal ions (Fe, La, Mo) [2], non-metal ions (N, C, Fe) [3] and co-doping (C-Cr, C-Mo) [4] to increase the photocatalytic and photovoltaic activity of TiO₂ materials. Xiao Q et al [5] studied that Ti ions substituted in metal or non-metal ions to improve the activity of TiO₂ photocatalytic. Gai et al [6] shown that TiO₂ band gap reduced by co-doping of C-Cr and C-Mo ion pairs. It is shown that the energy band gap of material reduced depending on the doping of TiO₂ material to fabricate the modification of TiO₂ in the visible light region. The photocatalyst activity can be enhanced by mixing metal oxide materials into pure semiconductor substances. Copper oxide is known as metal oxide or II-IV semiconductor which exhibits narrow bandgap. Yu et al [7] reported that the narrow bandgap was obtained by incorporating p-type semiconductors (CuO and CuO₂) into TiO₂ nanoparticles. Gray et al. [8] found that the ion of Cu

existed on the bulk mixture of CuO and TiO₂ to improve optical properties on the CuO-TiO₂. R. Marschall et al. [9] and H. Wang et al. [10] investigated the band position of CuO and TiO₂ on the CuO-TiO₂ system due to accumulation of charge carriers on CuO. Some reports have discussed the combination of wide-band-gap semiconductors (ZnO and TiO₂) and narrow bandgap (CuO) on the ternary (CuO/TiO₂/ZnO) [11] nanocomposites to improve the efficiency of photocatalytic activity. It was found that CuO is an oxide co-catalyst with the incorporation of TiO₂ and ZnO. Many researchers studied a lot of methods to improve photocatalytic efficiency under a visible light region. Among methods, the advantages of sol-gel methods have purity, homogeneity, felicity and flexibility in introducing dopants in a large concentration, stoichiometry control, ease of processing and composition control. Therefore, various CuO dosages on the doping of TiO₂ and ZnO material was mostly studied using a sol-gel method.

The present work studies the effect of CuO doping on the structural and optical properties of CuO-doped TiO₂ nanoparticles using sol-gel method.

2. Experimental Section

2.1. Materials

Titanium isopropoxide (C₁₂H₂₈O₄Ti, ≥97%, Sigma-Aldrich) was used as a starting material of TiO₂ nanoparticles. 1-butanol, glacial acetic acid (CH₃COOH, J.T Baker), sodium hydroxide (NaOH) and deionized water (DI) and ethanol were applied as a solvent. Copper sulphate pentahydrate (CuSO₄·5H₂O, 99%) was used as the dopant sources of CuO nanoparticles and CuO-doped TiO₂ nanoparticles. All analytical grade chemicals were used as received without any further purification.

2.2. Synthesis of CuO-doped TiO₂ Nanoparticles

Pure TiO₂ and CuO nanoparticles were prepared by using sol-gel method [12, 13]. In brief, titanium (IV)

isopropoxide solution (4 ml) was mixed with the solution of n-butanol (74 ml) and acetic acid (74 ml) under vigorous stirring. This is referred to the TiO_2 colloidal solution. Under stirring, 74 ml of deionized water was slowly added to the TiO_2 colloidal solution. After that, the solution was dried at 150°C for 2 h and calcined at 450°C for 2 h to obtain the TiO_2 nanoparticles. In order to synthesize CuO nanoparticles, 0.025 mol of $\text{CuSO}_4 \cdot 5\text{H}_2\text{O}$ was dissolved in 100 ml deionized water followed by the addition of 0.05 mol of NaOH in 150 ml deionized water under stirring. The solutions were heated at 80°C while stirring for 3h. Then, the precipitate was rinsed with deionized water and ethanol several times. Subsequently, the obtained precipitate was dried at 80°C for 4 h and annealed at 125°C for 8 h. CuO-doped TiO_2 nanoparticles with various mol% of CuO dopants were prepared by sol-gel method. First, the mixture of 0.0125 mol of NaOH in 65 ml deionized water was slowly added to a mixture of 0.0125 mol TiO_2 in 30 ml distilled water under stirring. The CuO nanoparticles (0.5, 1, 2, 3, 5, 10 mol%) were dissolved in 30 ml ethanol and continuously stirred at 80°C for 2 h. Finally, the products were repeatedly washed with ethanol and distilled water to remove the residual impurities. The obtained powder was aged in the air overnight and heated at 100°C for 1 h.

X-ray diffraction (XRD, Philips X' Pert MPD, Netherlands) was used to analyze the crystalline phase of the as-synthesized samples using Ni-filtered and Cu target from 20° to 90° at 80 mA and 40 kV. The crystallite size was calculated using Scherrer equation [14].

$$D = \frac{k\lambda}{\beta \cos \theta} \quad (1)$$

Where, λ is the Cu K α wavelength ($\lambda = 1.5418 \text{ \AA}$), β is the full width at half maximum of the diffraction angle, k is a shape factor (0.89) and θ is a diffraction angle. Field emission scanning electron microscope and scanning electron microscope (FE-SEM and SEM, FEI Quanta400, Czech Republic) with an accelerating voltage of 2 kV was employed to discover the morphology of the samples. The optical properties of CuO-TiO₂ nanocomposites were examined with Shimadzu UV-2450 UV-Vis spectrophotometer. The band gap energy was obtained by plotting Tauc equation with $(\alpha h\nu)^n$ versus $h\nu$ (2) to the photon energy axis [15].

$$(\alpha h\nu)^n = A (h\nu - E_g)^n \quad (2)$$

Where α is the absorption coefficient, h is a Planck's constant, ν is a photonic frequency, n is a direct semiconductor ($\frac{1}{2}$) and A is a proportional constant and E_g is optical band gap energy.

3. Results and Discussion

3.1. Effect of CuO Doping on Phase Composition of CuO-doped TiO_2 Nanoparticles

Figure 1. displays the XRD patterns of pure TiO_2 and different CuO dosages of 0.5-10 mol%. The diffraction peaks of pure TiO_2 (anatase phase) and CuO (monoclinic phase) were matched with the standard diffraction patterns of JCPDS 75-2547 and JCPDS 05-0661. At low concentrations of CuO dopants (0.5 mol% and 1 mol%), the diffraction peaks of TiO_2 anatase phase presented at 25.29°, 37.90°, 48.13°, 58.89°, 55.04°, 62.77°, 75.10° in corresponding to (101), (004), (200), (105), (211), (204), (215) planes, respectively. After high CuO concentrations (2 mol% to 10 mol%) was added, the mixture phase of anatase TiO_2 and monoclinic CuO was obtained. It was indicated that the CuO nanoparticles formed on the surface of TiO_2 in agreement with the expected data of Wan-Ting Chen et al [16]. The crystallite size in Table 1 revealed that the values calculated from the anatase TiO_2 phase peak at $2\theta = 25.29^\circ$ and monoclinic CuO phase peak at $2\theta = 35.53^\circ$ for all samples. The result showed that the crystallite size increased when the incorporation of CuO developed. The observation was in good agreement with the study of Siti Khalijah Kamarudin et al [17] that increasing CuO dosage results in an increase crystallite size. Therefore, CuO doping affected not only phase composition but also the crystallite size of CuO-doped TiO_2 nanoparticles.

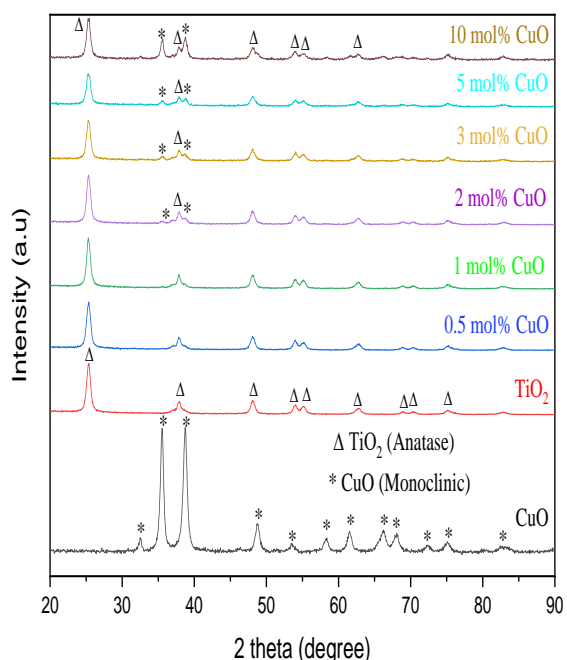


Figure 1. XRD Patterns of CuO-doped TiO_2 Nanoparticles with Various mol% Concentrations

Table 1. Crystallite Size and Band Gap Energy of CuO-doped TiO₂ Nanoparticles

Samples	Crystallite size (nm)		Absorption edge	Optical Band gap energy Eg (eV)
	TiO ₂ (Anatase)	CuO (Monoclinic)		
TiO ₂	17	-	395	3.26
0.5 mol% CuO	17	-	400	3.21
1 mol% CuO	20	-	405	3.19
3 mol% CuO	17	15	405	3.19
5 mol% CuO	22	18	410	3.10
10 mol% CuO	22	18	410	3.04

3.2. Effect of CuO Doping on Morphologies of CuO-doped TiO₂ Nanoparticles

Figure. 2 reveals the morphologies of pure TiO₂ and CuO-doped TiO₂ nanoparticles at 1mol% and 10 mol%. The morphology of pure TiO₂ nanoparticles (Fig. 2a) was equivalent to the spherical shape of TiO₂ nanoparticles. CuO-doped TiO₂ nanoparticles (Fig. 2b and c) consist of the spherical TiO₂ nanoparticles and clew-like CuO particles. The fewer agglomeration particles between CuO and TiO₂ occurred when CuO doping amount was low (Fig. 2b). As shown in Fig. 3, the peaks appeared the presence of Cu, Ti and O in 1 mol% CuO (Fig.2b). This indicates that the Cu²⁺ was dispersed over the TiO₂ at low CuO loadings. On the other hand, the formation of denser clew-like CuO particles was gradually formed although the slight aggregation of TiO₂ nanoparticles occur at increasing CuO doping (Fig. 2c). The change in morphological structure is in accordance with the resulted XRD showed in Fig. 1 that monoclinic CuO nanoparticles increased while anatase TiO₂ nanoparticles are still constant.

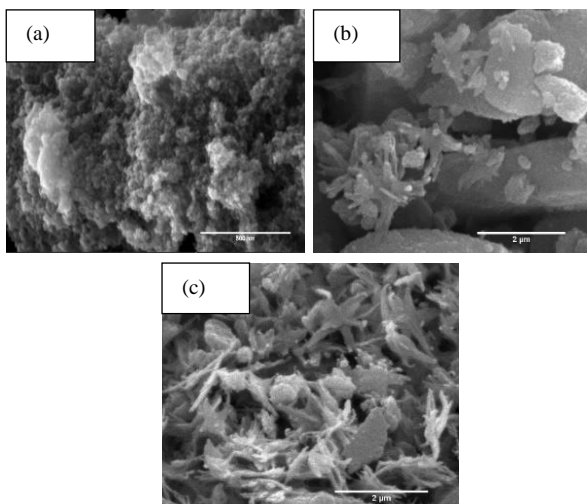


Figure 2. FESEM Image of (a) Pure TiO₂, SEM Images of (b) 1 mol% CuO and (c) 10 mol% CuO-doped TiO₂ Nanoparticles

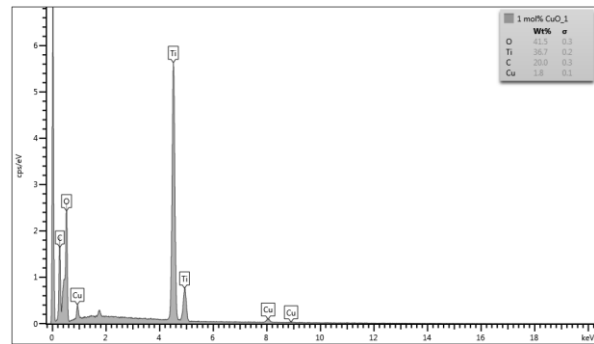


Figure 3. EDAX Spectra of 1 mol% CuO-doped TiO₂ Nanoparticles.

3.3. Effect of CuO Doping on the Optical Properties of CuO-doped TiO₂ Nanoparticles

Figure. 4a exhibits the absorption peak of undoped and doped CuO dopants on the TiO₂ surface. The absorption edge of pure TiO₂ (Figure. 4a) was obtained at 399 nm which is similar to the expected value of TiO₂ [18]. The values of the absorption edge and optical band gap energy are shown in Table 1. When CuO dopants added into the TiO₂, the absorption edge values changed according to the amount of doping CuO. The features of the absorption edge did not significantly shift at 0.5 mol% CuO dopants (Figure. 4b). At higher CuO doping (1 mol% and above) (Figure. 4c-f), the absorption edge increased into the extension of the visible region due to the attachment of CuO. This is due to the decrease in Fermi level between CuO and TiO₂ coupling bandgap [19]. Figure. 4b shows the band gap values of 0.5-10 mol% of CuO-doped TiO₂ nanoparticles. The results showed that the bandgap energy of doped CuO samples was lower than the undoped samples. Among increasing levels of CuO dopants, 10 mol% CuO decreased the bandgap energy values. This is due to the different electronic state of CuO²⁺ among increasing and decreasing CuO loading samples [20].

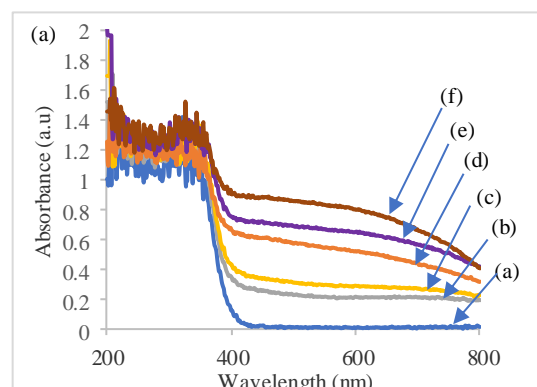


Figure 4. (a) UV-Vis Diffuse Reflectance Spectra of Pure (a) and CuO-doped TiO₂ (b) 0.5 mol%, (c) 1 mol%, (d) 3 mol%, (e) 5 mol% and (f) 10 mol%.

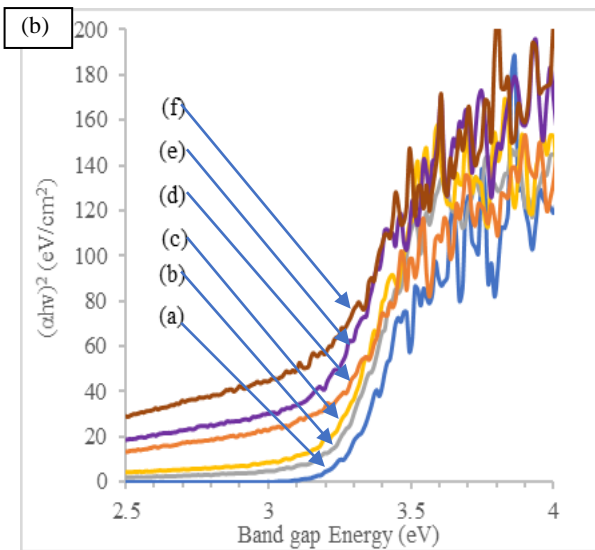


Figure 4. (b) The Band Gap Energy (eV) of Undoped, 0.5 mol%, 1 mol%, 3 mol%, 5 mol% and 10 mol% CuO-doped TiO₂ Nanoparticles.

4. Conclusion

CuO-doped TiO₂ nanoparticles were produced by using the sol-gel method with various mol% CuO doping. The dense structure of spherical and clew-like was achieved at CuO-doped on the TiO₂ nanoparticles. The phase of monoclinic and anatase mixture was obtained at 10 mol% CuO. CuO-doped TiO₂ nanoparticles had obviously increased crystallite size and reduced bandgap energy in the longer wavelength of absorption edge (400-800 nm). Among CuO doping, the optical bandgap of 10 mol% CuO was narrower than that of pure TiO₂ and other CuO samples. It was obvious that CuO doping altered a defining phase composition, crystallite size, morphology and optical property of CuO-doped TiO₂ nanoparticles.

5. Acknowledgement

This work was supported by Department of Mining and Materials, Faculty of Engineering at Prince of Songkla University (grant number ENG60021S).

6. References

- [1] C. Chen, W. Cai, M. Long, B. Zhou, Y. Wu, D. Wu and Y. Feng, "Synthesis of visible-light responsive graphene oxide/ TiO₂ composites with p/n Heterojunction", ACS publications, 4, 11, pp.6425-6432, 2010.
- [2] Y. Huo, J. Zhu, J. Li, G. Li and H. Li, "An active La/TiO₂ photocatalyst prepared by ultrasonication-assisted sol-gel method followed by treatment under supercritical conditions", Journal of molecular catalysis A: Chemical, 278, 1-2, pp.237-243, 2007.
- [3] X. Wang, S. Meng, X. Zhang, H. Wang, W. Zhong, and Q. Du, "Multi-type carbon doping of TiO₂ photocatalyst", Chemical Physics Letters, 444, 4-6, pp. 292-296, 2007.
- [4] C. Li, Y. Song, X. Yu, J. Liu, and J. Deng "Electronic structure and optical absorption spectra of C-Cr co-doped anatase TiO₂ based on first principles", Physical status solid B, 255, pp. 1700616, 2018.
- [5] Q. Xiao, J. Zhang, C. Xiao, Z. Si, and X. Tan "Solar photocatalytic degradation of methylene blue in carbon-doped TiO₂ nanoparticles suspension", solar energy, 82, 8, pp. 706-713, 2008.
- [6] Y. Gai, J. Li, S S. Li, J B Xia, and S H Wei, "Design of narrow-gap TiO₂: a passivated cooping approach for enhanced photoelectrochemical activity, 120, 3-23, pp.036402, 2009.
- [7] H. Yu, J. Yu, S. Liu and S. Mann, "Template-free Hydrothermal synthesis of CuO/Cu₂O composite hollow microspheres", Chemistry of materials, 19, 17, pp.4327-4334, 2007.
- [8] G. Li, N. M. Dimitrijevic, L. Chen, T. Rajh, and K.A. Gray, "Role of surface/interfacial Cu²⁺ sites in the photocatalytic activity of coupled CuO-TiO₂ nanocomposites", Journal of Physical Chemistry C 112, pp. 19040-19044, 2008.
- [9] R. Marschall, "Photocatalysis: semiconductor composites: strategies for enhancing charge carrier separation to improve photocatalytic activity", Advanced functional materials, 24, pp. 2421-2440, 2014.
- [10] H. Wang, L. Zhang, Z. Chen, J. Hu, S. Li, Z. Wang, J. Liu, and X. Wang, "Semiconductor heterojunction photocatalysts: design, construction, and photocatalytic performances", Chemical Society Reviews, 43, pp. 5234-5244, 2014.
- [11] A. Taufik, A. Albert, and R. Saleh, "Sol-gel synthesis of ternary CuO/TiO₂/ZnO nanocomposites for enhanced photocatalytic performance under UV and visible light irradiation", Journal of Photochemistry and photobiology A: Chemistry, 344, pp.149-162, 2017.
- [12] S. N. Muhith, B. D. Choudhury, M. T. Uddin and M. A. Islam, "Study of Photocatalysts for the treatment of dye-contaminated wastewater", International journal of integrated sciences and technology, 2, pp. 19-23, 2016.
- [13] Y. Aparna, K.V. E. Rao, P. Srinivasa, "Synthesis and characterization of CuO nanoparticles by novel sol-gel method", International Proceedings of Chemical, Biological and Environmental Engineering, 48, pp.156-160, 2012.
- [14] J. Huang, S. Wang, Y. Zhao, X. Wang, S. Wang, S. Wu, S. Zhang, and W. Huang, "Synthesis and characterization of CuO/TiO₂ catalysts for low-temperature CO oxidation", Catalysis Communications, 7, pp. 1029-1034, 2006.
- [15] W. Zhou, L. Gai, P. Hu, J.Cui, X. Liu, D. Wang, G. Li, H. Jiang, D. Liu, H. Liu, and J. Wang, "Phase transformation of TiO₂ nanobelts and TiO₂ (B)/anatase interface heterostructure nanobelts with enhanced photocatalytic

- activity” Crystal Engineering Communities 13, pp. 6643-6649, 2011.
- [16] W.T. Chen, V. Jovic, D. Sun-Waterhouse, H. Idriss, and G.I N. Waterhouse, “The role of CuO in promoting photocatalytic hydrogen production over TiO₂”, Hydrogen energy, 38, 2013, pp. 15036-15048.
- [17] S K. Kamarudin, N F. M.Yunos, B. Johar, S. Illias, and M A. Idris, “Effect of CuO doped TiO₂ on morphology, crystal structure and photocatalytic activity”, Journal of current science, engineering and technology, pp.239, 2018
- [18] R. Jaiswal, J. Bharambe, N. Patel, A. Dashora, D.C. Kothari, and A. Miotello, “Copper and Nitrogen co-doped TiO₂ photocatalyst with enhanced optical absorption and catalytic activity”, Applied Catalysis B: Environmental, 168-169, 2015, pp. 333-341.
- [19] A.L. Luna, M.A. Valenzuela, C. Colbeau-Justin, P. Vazquez, J.L. Rodriguez, J.R. Avendano, S. Alfaro, S. Tirado, A. Garduno, and J.M De la Rosa, “Photocatalytic degradation of gallic acid over CuO-TiO₂ composites under UV/Vis LEDs irradiation”, Applied Catalysis A: General, 521, 2016, 140-148.
- [20] Z. Liu and C. Zhou; “Improved photocatalytic activity of nano CuO- incorporated TiO₂ granules prepared by spray drying”, Progress in Natural Science: Materials International, 25, 2015, pp. 334-341.

The Analysis of Microstructure and Mechanical Property Relationship of a Standard Alloy Steel

Thet Wai Linn¹, Soe Lin Htike², Htein Win³

Faculty of Advanced Materials Engineering^{1,2,3}

University of Technology (Yatanarpon Cyber City)^{1,2,3}

Pyin Oo Lwin Township, Mandalay Region, Myanmar^{1,2,3}

linn.thet1@gmail.com¹, soelinnhtike11690@gmail.com², kohtein@gmail.com³

Abstract

The objective of this study is the analysis of the microstructure and mechanical properties of the alloy steel when subjected to various conditions of production heat treatment and service load. A commercial grade of F 10 T (M 22) steel bolts, nuts and washers was used in this study. The hardenability of tested steels was measured by the Jominy End-Quench test. This study has been found that thermal etching (TE) is the best technique to reveal the austenite grain boundaries in these steels. The main aim of this study is to analysis the microstructure and mechanical properties of alloy steels under different methods of heat treating process.

Keywords— Microstructure, Jominy End-Quench Test, Hardenability, Thermal Etching, Austenite Grain Boundaries.

1. Introduction

Steel is the most important engineering material and construction material. Steel fasteners, such as bolts, nuts and washers are utilized for a wide range of applications in the industries and steel structure. Steels with varying alloy contents and heat treatments were employed to measure the changes in microstructure and mechanical properties of high tension steel.

For heat treatment, hardenability is a very useful and important property of steel. It determines the rate at which the steel should be quenched. And also, it can know the maximum hardness that can be achieved on the cross section surface of steel bars, subjected to drastic quenching [1]. A steel of high hardenability will show a uniform, high hardness along the whole length of the bar. This is because the cooling rate, even at the far end of the bar, is greater than the critical cooling rate; and the whole bar transforms to martensite. The source of hardening is the formation and presence martensite structure. Thus high hardness is related to martensite formation. There are various methods to optimize the least expensive and most efficient alloy system. Quench factor analysis is also used to find hardness using data of Jominy end-quench test [2].

Due to its prominent influence on microstructure and mechanical properties, the accurate determination of the austenite grain size of materials becomes of the greatest importance in metallurgical studies [2]. The size

of the austenitic grains is the most important structural characteristic of heated steel. The austenitic grain size strongly effects its own transformation behavior and the mechanical properties of the microstructure formed from austenite [2]. Thus, the method of revealing austenite grain size is important in heat treatment of high tension fastener. The determination of the austenite grain size involves, in principle, two distinct stages: revealing the austenite grain boundaries and measuring their size. The austenite grain size is measured by ASTM (American Society of Testing Materials) grain size number [3].

2. Methodology

Hardenability of steel is defined as the susceptibility of the steel to hardening when quenched, and is related to the depth and distribution of hardness across a cross section [3]. There are various factors which effect hardenability of steels such as austenite grain size, carbon content and alloying elements percentage. There are various methods to measure hardenability of steel such as Grossman critical diameter method, Jominy-end quench test, estimation of hardenability from chemical composition and Fracture test [4]. Hardenability is a measure of the depth to which steel will harden when quenched from its austenitizing temperature. It is measured quantitatively, usually by noting the extent or depth of hardening of a standard size and shape of test specimen in a standardized quench. In this experiment, Jominy end-quench test is used to measure the hardenability of the steel Figure.1 [5].

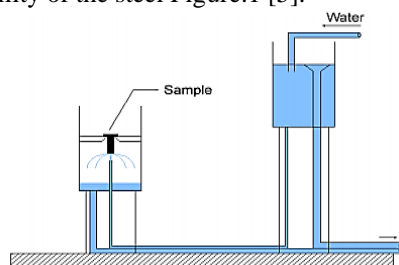


Figure 1. Layout of Jominy End-Quench Test [5]

Many properties of materials depend on the grain size and the shape of grains. The austenitic grains size is an important specification of steels as this size determines many properties which are of significant importance in steels, which are hardened. The austenitic grain size strongly effects its own transformation behavior and the mechanical properties of the

microstructures formed from austenite. Austenitic grain boundaries are preferred size for the nucleation of proeutectoid phases and pearlite, which are diffusion controlled transformation products. Austenite is a high temperature phase (except in some alloy steels), and is no longer present when metallographic examination is made, but it is decomposed to aggregate of ferrite and carbide, or martensite.

This study has been carried out over a wide range of temperatures (900–1000°C) and it has been found that thermal etching (TE) is the best technique to reveal the prior-austenite grain boundaries in these steels. Thermal etching method is heating up to the austenitization temperature a sample with a finely polished surface in a vacuum with a pressure of at least 1Pa or in an inert atmosphere^[6]. After austenitization, samples are cooled down to room temperature. The resulting austenite grain size determined by Jefferies Planimetric Test [7].

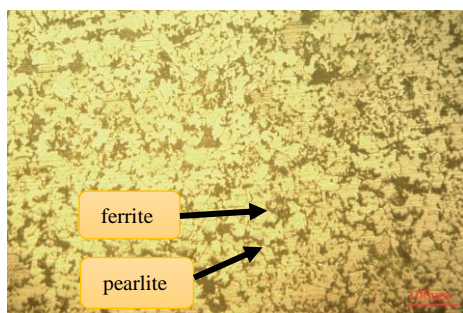
3. Experimental Procedure

3.1. Materials

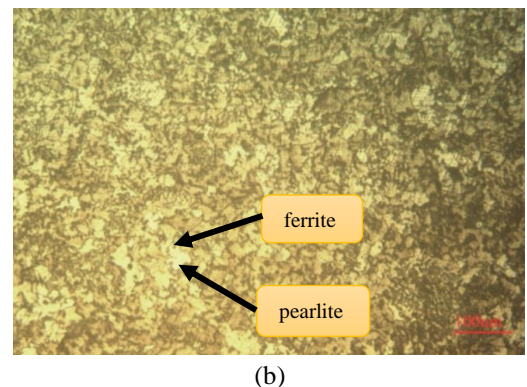
The tested raw steel was received from the Steel Melting Shop of No. (3) Steel Mill (YWAMA). It was commonly used for fasteners. The chemical composition (wt. %) was determined by Optical Emission Spectrometer (OES) and listed in Table 1. Figure .2(a) and (b) show the original microstructure of tested steel. The tested material was cut from the raw steel. Sample was manually grind with emery papers and polished with diamond paste and then etched in a Nital solution (2% nitric acid+ 98% alcohol) for 5s. It consisted of ferrite and small amount of pearlite.

Table 1. Chemical Composition of Test Material (wt %)

Elements	Wt %
C	0.294
Si	0.158
Mn	0.722
P	0.004
S	0.002
Al	0.013
B	0.002



(a)



(b)

Figure 2. Microstructure of the Test Steel at a Magnification of 100× (a) Longitudinal Section; Showing Banded Structure, ie. Pearlite Grains Lying Along the Rolling Directions (b) Transverse Section; Showing Equiaxed Grains and Homogenous Distribution of Ferrite and Pearlite.

3.2. Hardness Testing

In hardness testing, the raw specimen was prepared and took five test points on the specimen with a transverse distance by using Rockwell Hardness Tester (HRC). The result obtained in hardness testing is shown in Table 2.

Table 2. Hardness Test Result

Position	Hardness (HRC)
1	18.38
2	17.67
3	17.96
4	18.92
5	19.34
Average	18.454

3.3. Hardenability of Steel Using Jominy End Quench Test

(1) Preparation of Test Specimen and Apparatus for Jominy End-Quench Test: In the Jominy end-quench test, a slightly oversize bar (1.5 in) diameter of steel sample was normalized at about (40-60°C) above AC_3 temperature for 1hr [2]. After that, this steel sample was machined to the size of 4 in long and 1 in diameter as shown in Figure.3. Machining removes any decarburized layer formed in the normalizing treatment [7]. The standard test methods are contained in specifications of the American Society for Testing and Materials (ASTM Method A-255).

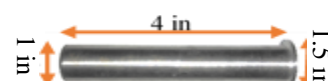


Figure 3. Jominy End-Quench Test Steel Bar

Jominy end-quench apparatus is shown in Figure.4. In this device, the diameter of the pipe opening is $\frac{1}{2}$ inch. Specimen holder is such that the bottom of the specimen remains at $\frac{1}{2}$ inch above the nozzle [8]. The constant

pressure of the water is such that the high of the unimpinged jet is 2 ½ inch.



Figure 4. Jominy End-Quench Apparatus

(2) *Heating:* Place the sample steel bar in electric heat treating furnace at the specified austenitizing temperature (900°C) and hold at this temperature for 45 min. After austenitizing, Jominy bar is transferred to the quenching device. The stream of water is then directed against the bottom face of the specimen for not less than 10 minutes. While doing the quenching, a condition of still air is maintained around the specimen. Quenching operation consists of cooling one end of the jominy-bar by a jet of water. The Jominy-bar after quenching is then prepared for the hardness measurements by surface grinding machine [3].

3.4. Revealing Austenite Grain Boundaries of Steel Using Thermal Etching

Cylindrical samples of 5 mm in diameter and 12 mm in length were used to reveal grain boundaries by thermal etching method as shown in Figure 5. After that, a 2 mm wide surface was generated along the longitudinal axis of samples was manually grind with emery papers and carefully polished with 3 µm diamond paste. Later on, those samples were heat treated in the vacuum furnace. After reaching a vacuum pressure higher than 1 Pa (minimum value advised to avoid too much oxidation on the polished surface), samples were heated at a rate of 30°C/min at the austenitization temperatures 1000°C and holding times is 5 min (300 s). Subsequently, samples were cooled down to room temperature at a cooling rate of 30°C/min. And then, the heat treated samples were observed using metallurgical microscope. This tested sample under thermal etching do not require any metallographic preparation after heat treatment. The prior austenite grain boundaries are revealed without chemical etching [4].



Figure 5. Test Specimen for Thermal Etching

4. Results and Discussion

4.1. Hardness Test

Rockwell Hardness Tester (HRC) results of sample at five test points are 18.38, 17.67, 17.96, 18.92, 19.34 respectively. The average hardness is 18.454 HRC.

4.2. Hardenability Test

Hardness was measured with distance from the quenched end using the Rockwell hardness testing machine. The test specimen was moved accurate steps of 1/16 in. (1.5mm) from the quenched end. Readings were taken in steps of 1/16 in. (1.6 mm) for the first sixteenths (25.4mm), then 18, 20, 22, 24, 28, 32, 48 and 64 of an inch [3]. The hardness test results are shown in Figure 6.

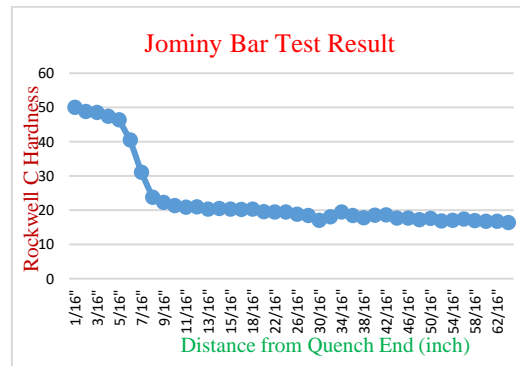


Figure 6. Jominy Bar Hardness Test Result

(1) *Index of Hardenability:* The hardenability of a tested steel can be designated by a specific HRC hardness value at a given Jominy (J) distance.

(2) *Calculation of Hardenability:* This method of Jominy Hardenability calculation from the chemical ideal diameter (DI) on a steel is based on the original work of M. A. Grossman and provides increased accuracy by refinement of the carbon multiplying factors and the correlation of a boron factor (B.F) with carbon and alloy content. The effects of phosphorous and sulfur are not considered since they tend to cancel one another. For DI calculation, the required data are shown in Table 3.

Table 3. DI Calculation is given as follows for Tested Steel

Element	%	Multiplying Factor
Carbon	0.294	0.157
Manganese	0.722	3.400
Silicon	0.158	1.112
Boron	0.001	-
Aluminum	0.013	-
Phosphorous	0.004	-
Sulfur	0.002	-

Where:

$$DI = 0.157 \times 3.400 \times 1.112 = 0.593 \sim 0.6 \text{ in (excluded boron)}$$

(3) *DI Calculation for Boron Steel:* The boron factor (signifying the contribution for boron to increased hardenability) is an inverse function of the carbon and alloy content. The higher the carbon or alloy content, or both, the lower the boron factor. The actual boron factor is expressed by the following relationship:

$$B.F = \frac{\text{measured DI (from Jominy data and carbon content)}}{\text{calculated DI (from composition excluding boron)}}$$

An actual boron factor determination is given as follows for tested steel and End-Quench test results showed in Table 4.

Table 4. End-Quench Test Result (in)

J position (1/16 in)	HRC
1	50
3	48.5
5	46.4
7	31
9	22.1
12	20.9
14	20.5
16	20.2
18	20.3

Using Table 5, (Carbon Content, Initial Hardness, 50% Martensite Hardness) from ASTM A-225 [3]. Using Table 3, determine the nearest location on the end-quench curve where hardness corresponding to 50% martensite occurs for the actual carbon content. The tested heat with 0.29 carbon, this hardness is 37 HRC occurring at a "J" distance of 8/16 from the quenched end.

Table 5. Carbon Content, Initial Hardness, 50 % Martensite Hardness [3]

Carbon Content (%)	Hardness - HRC	
	Initial Martensite (100%)	Martensite (50%)
0.20	44	32
0.21	45	32
0.22	45	33
0.23	46	34
0.24	46	34
0.25	47	35
0.26	48	35
0.27	49	36
0.28	49	36
0.29	50	37

From Table 6, a "J" distance of 8/16 in, equates to a measured DI of 2.97 in.

Table 6. Jominy Distance for 50% Martensite Versus DI [3]

"J" 1/16 in.	DI, in.	"J" 1/16 in.	DI, in.	"J" 1/16 in.	DI, in.
0.5	0.27	11.5	3.74	22.5	5.46
1.0	0.50	12.0	3.83	23.0	5.51
1.5	0.73	12.5	3.94	23.5	5.57
2.0	0.95	13.0	4.04	24.0	5.63
2.5	1.16	13.5	4.13	24.5	5.69
3.0	1.37	14.0	4.22	25.0	5.74
3.5	1.57	14.5	4.32	25.5	5.80
4.0	1.75	15.0	4.40	26.0	5.86
4.5	1.93	15.5	4.48	26.5	5.91
5.0	2.12	16.0	4.57	27.0	5.96
5.5	2.29	16.5	4.64	27.5	6.02
6.0	2.45	17.0	4.72	28.0	6.06
6.5	2.58	17.5	4.80	28.5	6.12
7.0	2.72	18.0	4.87	29.0	6.16
7.5	2.86	18.5	4.94	29.5	6.20
8.0	2.97	19.0	5.02	30.0	6.25
8.5	3.07	19.5	5.08	30.5	6.29
9.0	3.20	20.0	5.15	31.0	6.33
9.5	3.32	20.5	5.22	31.5	6.37
10.0	3.43	21.0	5.28	32.0	6.42
10.5	3.54	21.5	5.33		
11.0	3.64	22.0	5.39		

$$B.F = \frac{\text{measured DI (from Jominy data and carbon content)}}{\text{calculated DI (from composition excluding boron)}}$$

$$\text{Boron Factor} = \frac{2.97 \text{ in}}{0.6 \text{ in}} = 4.95 \text{ boron factor}$$

$$\text{Alloy Factor} = \frac{\text{Calculated DI (without boron)}}{\text{Carbon multiplying factor}}$$

$$\text{Alloy Factor} = \frac{0.6 \text{ in}}{0.157 \text{ in}} = 4$$

And then, boron multiplying factor from the standard. The carbon 0.29% and an alloy factor of 4, the boron multiplying factor is 2.595 (interpolation required). Then, DI with boron is:

$$DI_B = DI \text{ (without boron)} \times \text{boron factor}$$

$$DI_B = 0.6 \text{ in} \times 2.595$$

$$DI_B = 1.557 \text{ in}$$

Thus, the ideal critical diameter for tested steel is 1.557 in.

Using jominy curve, the result between 5/16" and 7/16" can be the critical cooling rate. This test is finding which distance can be formed 50% martensite structure and which is used to measure the hardenability of the steel. The standard testing steel is the high strength structural steel and this steel must have high hardenability. And, this testing procedure is to find the corresponding diameter and the result critical diameter is 1.557 in. Thus, this diameter can be used to have high hardenability in production of fastener in a given steel.

Ideal Critical Diameter for Diameter in real quenching medium can find by using Figure.7 where the ideal critical diameter D_I is plotted as the abscissa, and the critical diameter D is plotted as the ordinate. Some of the values of this number for commercial quenches are given in Table 7. And the result real diameter is D value 0.75 for strong oil quench and D value 0.85 for poor

water quench [8]. Using the resulting real diameter, which combination of diameter and quenching media can be used in hardening.

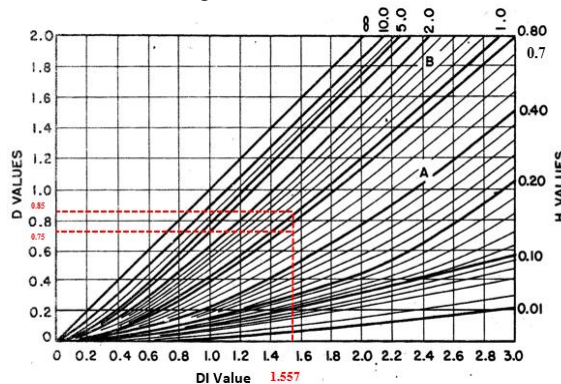


Figure 7. Relationships among Ideal Diameter, Critical Diameter and Severity of Quench [8]

Table 7. Severity of Quench Values for Some Typical Quenching Conditions [8]

H Value	Quenching Condition
0.20	Poor oil quench - no agitation
0.35	Good oil quench - moderate agitation
0.50	Very good oil quench - good agitation
0.70	Strong oil quench - violent agitation
1.00	Poor water quench - no agitation
1.50	Very good water quench - strong agitation
2.00	Brine quench - no agitation
5.00	Brine quench - violent agitation
∞	Ideal quench

Alloy content are mostly depend in hardenability of a given steel and this alloy content affect in this steel especially boron. One reason for adding boron in alloying element is to increase the hardenability of steel. Boron content of 0.0005% to 0.003% has relatively large and optimum effect (the testing steel have boron 0.002%). Boron may form borocarbide, $Fe_{23}(C, B)_6$ at austenite grain boundaries. Boron can segregates to grain boundaries of austenite and thus, retard the nucleation of pearlite and ferrite. Thus boron is added in alloying element to have refine grain size. Fastener standard grade for high tension steel must have a range between 27 to 38 HRC (bolt), 25 to 30 HRC (nut) and 35 to 45 HRC (washer) and this experimental procedure conclude which temperature, time and quenching media can be used to get the standard grade range.

4.2. Measuring Austenite Grain Size

After the austenite grain boundaries was revealed, the austenite grain size can be determined by Jefferies Planimetric Test. Fig.8 show the measurement of ASTM grain size number and it grain size number is 6.6528.

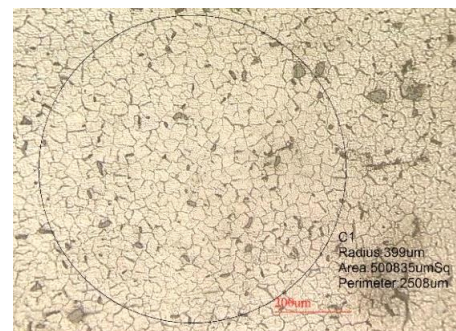


Figure 8. Jefferies Planimetric Test for ASTM Grain Size at 100 X

Grain boundaries are the preferential nucleation sites for ferrite and pearlite. If austenite grain size is large, the grain boundary area decreases. This means that nucleation sites are being reduced in number. The large austenite favor to formation of pearlite and ferrite because of its surface area and small austenite detect the formation of ferrite and pearlite in boundaries.

The specification of the steels include the grain size too and it helps in assessing the quality or steel, or its heat treatment. Steel with ASTM grain size number below 3 identified coarse grain steel and above 6 means a fine grain steel. Above ASTM No 8 are ultra-fine grain steel. Case hardening steels usually have fine grain of ASTM 5 to 8. Quenched and tempered tool steels have grain size not coarser than ASTM7. High speed steel after hardening have ASTM9-10. The standard grade for this testing steel for structural fasteners is ASTM grain size 6, 7 and 8 [2]. Thus, the testing result ASTM grain size is between the recommend range and this grain size is assist to determine the hardening temperature and time during heat treatment circles.

5. Conclusion

In this paper, Jominy test help to find ideal critical diameter and help to find suitable quenching medium. The microstructural changes are related to the variations of the cooling rate. The data from Jominy test and combination with alloy content can be used to determine this steel can be sufficiently hardened for a given application. The tested procedures based on the combination of heat treatment and thermal etching revealed the austenite grain boundaries of steel which verify the correct heat treating time and temperature of the present practice at the factory. It is recommended that the steel composition (JIS B 1186) is suitable to production the fasteners for the given applications.

6. References

- [1] Robert E. Reed-Hill. 1973. "Physical Metallurgy Principles". Second edition.
- [2] Singh. V, Delhi. 1998. Standard Publishers Distributors, "Heat Treatment of Metals".
- [3] ASTM A225-99, "Standard Test Methods for Determining Hardenability of Steel".
- [4] Albert G. Guy. 1967. "Element of Physical Metallurgy". Second edition.
- [5] Bhaskar Chandra Kandpal, Agnay Chutani, Amit Gulia, Harsimran, Chandan Sadanna, 2011. International Journal of Advances in Engineering & Technology, "A Review on Jominy Test and Determination of Effect of Alloying Elements on Hardenability of Steel Using Jominy End Quench Test".
- [6] C. Garcí'a de Andre's. 2001. "Metallographic techniques for the determination of the austenite grain size in medium-carbon microalloyed steels".
- [7] ASTM E112-96, "Standard Test Methods for Determining Average Grain Size".
- [8] Donald R. Askeland, Pradeep P, Fulay. 2009. "Essentials of Materials Science and Engineering", Second edition.

Evaluation of the Performance of Various Corrosion Inhibitors on Mild Steel

Shwe Wut Hmon Aye¹, Waing Waing Kay Khaing Oo²

Department of Metallurgical Engineering and Materials Science^{1,2}

West Yangon Technological University^{1,2}

Hlaing Thar Yar Township, Yangon Region, Myanmar^{1,2}

hmon152@gmail.com¹, waingkaykhine@gmail.com²

Abstract

The performance of anodic and cathodic corrosion inhibitors on mild steel were investigated by using the linear sweep voltammetry (LSV) and electrochemical impedance spectroscopy (EIS). It was observed that efficiency increases with inhibitor concentration up to the optimum level used in cathodic inhibitor. It was also observed that the lower corrosion currents can be found in the solution that used anodic inhibitors. Among the anodic inhibitors, cerium nitrate appears to provide more long term corrosion inhibition.

Keywords- Corrosion, Inhibitor, Anodic inhibitors, Cathodic inhibitors, Electrochemical methods

1. Introduction

Mild steel is a type of carbon steel with a low amount of carbon (less than 0.3 percent) and it is also called low carbon steel or plain carbon steel. The properties such as good mechanical strength, good ductility of mild steel such as is very effective for many applications. As a result of its versatility and low cost to produce, this material has grown to become one of the most common forms of steel available on the market. Much of the mild steel that is manufactured is exposed to outdoor conditions, often in highly polluted atmospheres where corrosion is more severe than in other environments.

Corrosion is an electrochemical process which is one of the most notable causes of metal degradation. Therefore, it continues to be the subject of extensive studies with a view to its minimization in order to extend the lifetime of metals. From the studies it can get different possibilities to protect from corrosion: stainless steel, sacrificial protection, application of protective layers and corrosion inhibitors.

Corrosion inhibitor is the substance which reduces the corrosion rate of the metal that exposed their environment [2]. The main purpose of using inhibitors is to prevent the dissolution of metal due to corrosion. Inhibitors can absorb the metal surface through the interaction between metal and environments [1]. Corrosion inhibitors are made of different organic and inorganic compounds such as molybdates, phosphates, silicates and triazoles and others. There are different types of corrosion inhibitors such as anodic inhibitors, cathodic inhibitors, mixed inhibitors and volatile corrosion inhibitors.

Anodic inhibitors are chemical substances that absorb onto the metal substance and form the protective layer of the oxide film on the metal surface. Connected with the inhibition is a shift of the free corrosion potential. The shift is towards more positive potential for anodic inhibitors [7]. Cathodic inhibitors are also the chemical substances that slow the cathodic reaction (oxygen reduction) itself or selectively precipitate on the cathodic sites and limit the diffusion of reduced species. Corrosion potential is shift towards to more negative values in cathodic inhibitors. The selection of suitable inhibitors depends upon many factors such as economic availability, environmental side effects, concentration, temperature, type of acid, the presence of dissolved inorganic and/or organic substances even in minor amounts and of course on the type of metallic materials supposed to be protected.

The aim of this study is to evaluate the performance of various corrosion inhibitors on mild steel based on some electrochemical methods such as Linear Sweep Voltammetry (LSV) (to select the most efficient corrosion inhibitor and its concentration) and Electrochemical Impedance Spectroscopy (EIS) (to build an equivalent circuit model in order to get information about the corrosion inhibition mechanism). In literature reviews, benzothiazoles compounds, cerium salts and molybdates (environmental friendly corrosion inhibitor) have been mainly used as effective corrosion inhibitors for steel and various metal alloys [3, 4, 8]. So, in this work Mercaptobenzothiazole is used as the cathodic inhibitor and cerium nitrate and sodium molybdate are used as the anodic inhibitor.

2. Experimental Procedure

The required processes are carried out as followings. The first step is sample and solution preparation and the second step is studying on electrochemical measurements.

2.1 Sample and Solution Preparation

All electrochemical measurements were performed on mild steel (SAE 1010). Firstly all samples were cleaned with ultrasonic bath till 30 minutes. After cleaning, the sample was washed with deionized water and then dried in the oven. 5.08cm² was leaved for working area and other sides areas were sealed with green tape. Then the sample was stored in the desiccator to prevent the moisture.

0.1M NaCl solution was prepared with analytical grade sodium chloride and deionized water firstly. Electrochemical measurements were performed in 0.1M NaCl solution with the inhibitor free and the presence of various concentrations of anodic and cathodic inhibitors. The different concentrations of inhibitors were obtained by diluting the correct amounts of this solution to obtain 0.000001M, 0.00001M, 0.0001M, 0.001M solutions respectively.

2.2 Electrochemical Measurements

All electrochemical measurements were carried out at 25°C using an Autolab 302N potentiostat with FRA (frequency response analyzer). Conventional three electrode set up was used and opened to atmosphere. Mild steel (SAE 1010) was used as the working electrode, saturated silver-silver chloride was used as the reference electrode and platinum grid was used as the counter electrode. Firstly corrosion behaviour of mild steel was investigated with linear sweep voltammetry (LSV) measurement. Measurement was carried out after one hour immersion time and the sample was polarized cathodically and anodically separately from -780mV to 380mV with 10mV/s scan rate. Electrochemical impedance spectroscopy was measured after 20 minutes and 2 hour immersion of working electrode. Total impedance Z and phase shift Q were measured in the frequency range from 1MHz to 10⁻² Hz with 10mV/s single amplitude perturbation (peak to peak). In all experiments, the Bode diagrams were fitted using the Zview program.

3. Results and Discussions

To know the performance of various corrosion inhibitors on mild steel, two electrochemical techniques were studied. The first technique is linear sweep voltammetry and the second one is single sine impedance spectroscopy. In this study, the corrosion current of mild steel is characterized by studying the oxidation reaction (mild steel dissolution) and reduction reaction (oxygen reduction).

3.1 Results of Linear Sweep Voltammetry

Linear sweep voltammetry measurements allow determining condition of the corrosion inhibition of mild steels. Polarization curves (also “Tafel plots”) of different corrosion inhibitors on mild steel samples were recorded and compared in order to find the most efficient corrosion inhibitors. Polarization curves of different inhibitors concentrations (0.000001M, 0.00001M, 0.0001M and 0.001M) after one hour optimum corrosion potential (OCP) are shown in figure 1. Figure 2 shows the extrapolation of liner part of cathodic and anodic polarization curves of mild steel.

The interception point of cathodic and anodic polarization curves show corrosion potential and

corrosion current density of mild steel. In Figure 1, it was showed that corrosion potential of anodic inhibitors [Na₂MoO₄ and Ce (NO₃)₃] that used in the solution shifts to more positive values than that of cathodic inhibitors (MBT). And it was also observed that the lower corrosion currents could found in the solution that used anodic inhibitors. It was cleared that corrosion rate of mild steel sample that immersed in the anodic inhibitors was lower and better inhibition effects are observed after 1 hour immersion time.

According to the data, anodic inhibitors [Na₂MoO₄ and Ce (NO₃)₃] are best efficient inhibitors for mild steel after one hour immersion time. Among the anodic inhibitors, corrosion current of Na₂MoO₄ is the lowest.

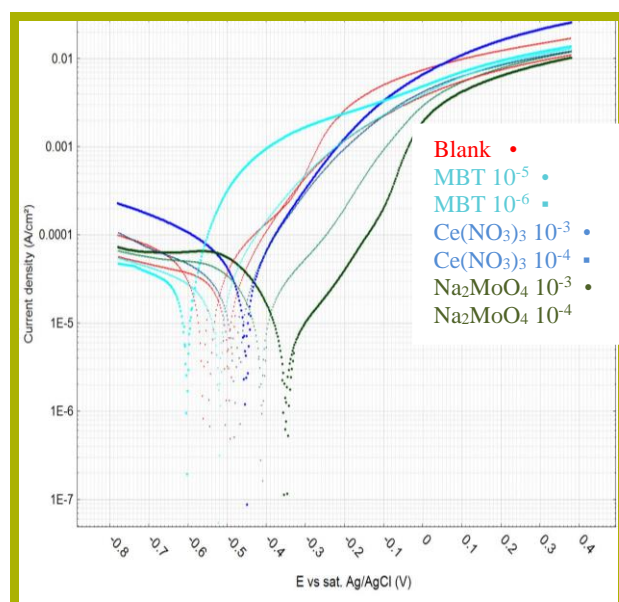


Figure 1. Polarization Curves of Different Inhibitors Concentrations

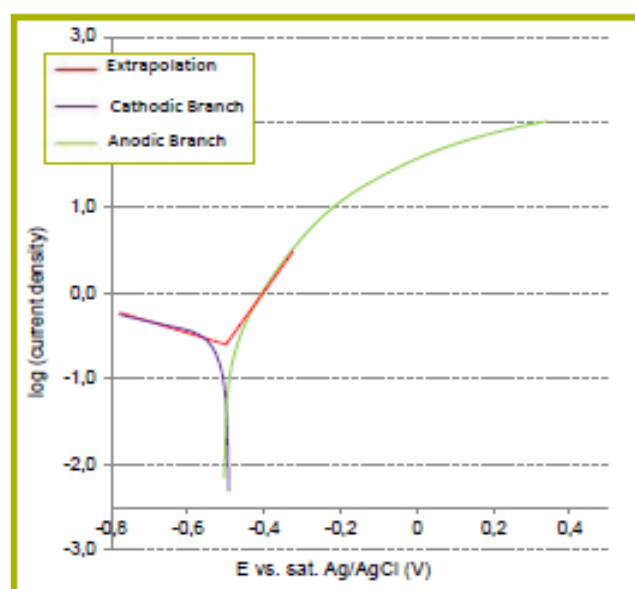


Figure 2. Extrapolation of Liner Part of Cathodic and Anodic Polarization Curves of Mild Steel

3.2 Calculations of Inhibitor Efficiency Based on Different Type of Inhibitors

To know the inhibitor efficiency , it is needed to calculate by using the following equation.

Inhibitor Efficiency (%) = $(CR_{\text{uninhibited}} - CR_{\text{inhibited}}) \times 100$ where $CR_{\text{uninhibited}}$ = corrosion rate of the uninhibited system, $CR_{\text{inhibited}}$ = corrosion rate of the inhibited system [9].

Table 1.Relation between Corrosion Current Density and Inhibitor Efficiency

Corrosion inhibitor	Corrosion potential (V)	Corrosion current density (10^{-5}A/cm^2)	Inhibit or Efficiency (%)
Blank	-0.498	2.62	0
MBT 10^{-5}M	-0.607	2.82	-7.65
MBT 10^{-6}M	-0.512	2.07	20.93
Cen(NO_3) $_3$ 10^{-4}M	-0.453	1.54	41.25
Ce(NO_3) $_3$ 10^{-3}M	-0.448	1.37	47.64
Na_2MoO_4 10^{-4}M	-0.418	1.11	57.73
Na_2MoO_4 10^{-3}M	-0.350	0.52	80.18

According to the table 1, the inhibitor efficiency of MBT was negative effect when the concentration was increased the optimum level. The inhibitor efficiency of sodium molybdate with 0.001M solution was higher and corrosion current density was lower than others. So it was also confirmed that sodium molybdate was most suitable for mild steel to get best inhibition efficiency after one hour immersion time. These results are shown in Figure 3.

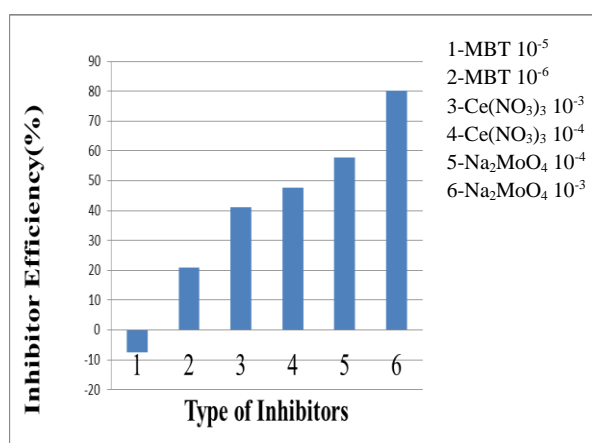


Figure 3. Inhibitor Efficiency Based on Different Type of Inhibitors

3.3 Results of Electrochemical Impedance Spectroscopy (EIS)

The corrosion inhibitors which showed the best efficiency (Na_2MoO_4 and $\text{Ce}(\text{NO}_3)_3$) in the LSV-experiments were taken into further study with EIS. In EIS measurements, the corrosion behaviour was studied after 20 minutes and 2 hours immersion.

Electrochemical impedance spectroscopy was used to study the behavior of metal/solution interface in the absence and in the presence of inhibitor [1]. The Bode and phase angle plots for mild steel in 0.1M NaCl with and without inhibitors are shown in Figure 4 and 5. According to the data, it was observed that highest impedance value of anodic inhibitors form at low frequencies in 20 minutes and 2 hour immersion. Among the anodic inhibitors, the impedance value of Na_2MoO_4 with 0.0001M was highest in 20 minutes immersion.

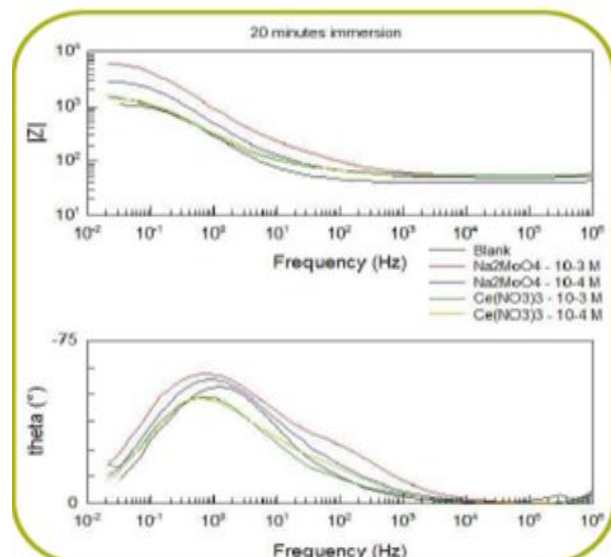


Figure 4. Bode Plots after 20 Minutes Immersion

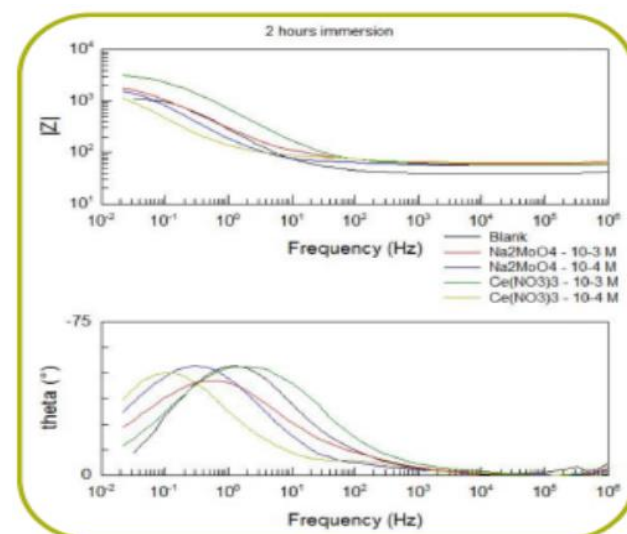


Figure 5. Bode Plots after 2 Hours of Immersion

During this time the inhibitors covered the metal surface by the physical interaction, depressed the corrosion reaction occurring on the metal surface by the chemical interaction and then reduced the corrosion rate of the metal. The Bode phase angle plots show single maximum (one time constant) at intermediate frequencies for the corrosion process at the metal-solution interface. The increase in the peak heights indicates a more capacitive response of the interface due to the presence of inhibitor molecules at the interface. In Figure 4 and 5 the highest peak height of Na_2MoO_4 was observed in 20 minutes immersion time and that of $\text{Ce}(\text{NO}_3)_3$ was highest in 2 hour immersion time. But the inhibition efficiency of Na_2MoO_4 was decreased in 2 hour immersion time. It might be the steel sites became fully cover increment of inhibitor and it can't change inhibition efficiency when the immersion time is increased. But inhibition efficiency of $\text{Ce}(\text{NO}_3)_3$ is still increasing in 2 hour immersion. Ce^{3+} ions can absorb onto the metal surface. Then it form a thick film on the metal surface that composed of a porous outer layer and more compact inner layer with high corrosion resistance.

To better understand the corrosion of the mild steel, the impedance data were modeled with the electrical equivalent circuits (EEC) shown in Figure 6, in which R_{el} is the resistance of the electrolyte, R_{pores} is pore resistance, R_{corr} is corrosion resistance, CPE_{dl} is the constant phase element of the double layer and CPE_{ox} is the constant phase element of the oxide layer.

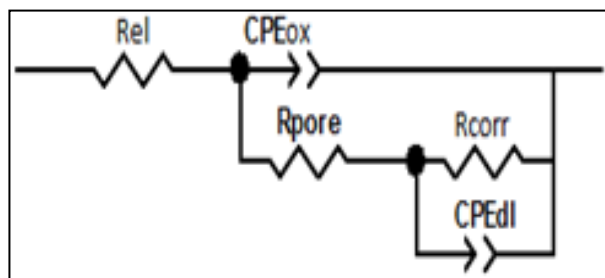


Figure 6. Equivalent Circuit Model

The double layer and oxide layer capacitances are, therefore, modelled with a CPE that accounts for the imperfections of the surface. The impedance of the CPE is formulated as a function of the frequency f with the Q and α parameters according to $Z_{CPE} = 1 / [Q \cdot (j \cdot 2\pi f)^\alpha]$. The evolved data after immersion of anodic inhibitors with different concentrations are shown in Figure 7.

The data shown in Figure 7 reveals that the value of corrosion resistance of sample that immersed in Na_2MoO_4 is increased among others in 20 minutes immersion time. In 2 hour immersion time, corrosion resistance of sample that immersed in $\text{Ce}(\text{NO}_3)_3$ is the highest. According to the results, the fitting analysis data is equal to the experimental data.

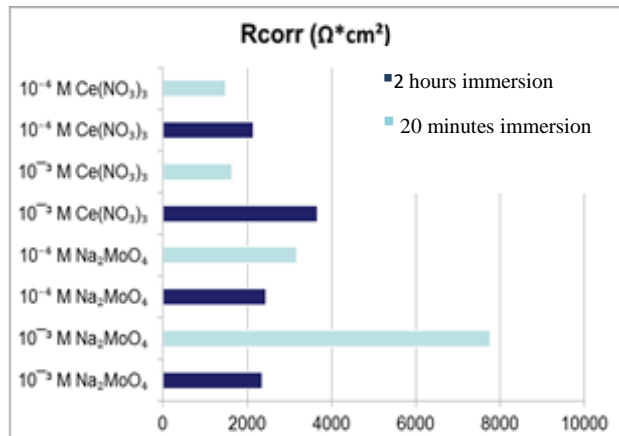


Figure 7. Corrosion Resistance with Different Anodic Inhibitors

The comparison of corrosion behaviour of the sample surface with and without inhibitors after 2 hours immersion is shown in Figure 8. The least corrosion product was found in the sample that used in $\text{Ce}(\text{NO}_3)_3$ 10^{-3} M . This result is also aligned with the EIS results.

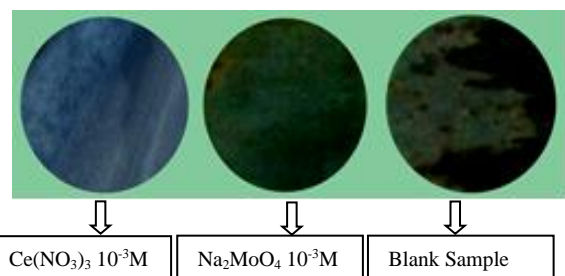


Figure 8. Photographs of Corroded Samples after 2 hr Immersion

4. Conclusions

In this work, linear sweep voltammetry (LSV) and Electrochemical impedance spectroscopy measurements were successfully integrated to evaluate the performance of various corrosion inhibitors on mild steel. According to the data, efficiency increases with inhibitor concentration up to the optimum level. That is clearly seen for MBT. Anodic inhibitor (Na_2MoO_4) is the highest efficiency after 20min and 1h immersion time. Inhibition efficiency of Na_2MoO_4 is decreased after two hours immersion time. Inhibition efficiency of $\text{Ce}(\text{NO}_3)_3$ is lower after 20min and 1h immersion time. Still 2 hrs, inhibition efficiency of $\text{Ce}(\text{NO}_3)_3$ is increasing. Inhibiting properties are also to be seen optically. Therefore, $\text{Ce}(\text{NO}_3)_3$ appears to provide more long term corrosion inhibition by using the laboratory accelerated testing devices.

5. References

- [1] Dariva, C.G., Galio, A.F. (2014), Corrosion Inhibitors – Principles, Mechanisms and Applications, *Developments in Corrosion Protection*, 365-376.
- [2] Fatai Olufemi ARAMIDE, Corrosion Inhibition of AISI/SAE Steel in a Marine Environment, *Leonardo Journal of Sciences* 2009, Issue 5, P.47-52.
- [3] Kakaroglou, A; Domini, M; De Graeve, I. Encapsulation and incorporation of sodium molybdate in polyurethane coatings and study of its corrosion inhibition on mild steel, *Surf. Coat. Technol.* 2016, 303,330-341
- [4] K.Parameswari, S.Chitra, A. Selvaraj, S.Brindha and M. Menaga, Investigation of Benzothiazole Derivatives as Corrosion Inhibitors for Mild Steel, *Portugaliae Electrochimica Acta* 2012, 30(2), 89-98
- [5]Sherif, E.M., Erasmus, R.M., Comins, J.D. (2010), In situ Raman spectroscopy and electrochemical techniques for studying corrosion and corrosion inhibition of iron in sodium chloride solutions, *Electrochimica Acta*, 55, 3657-3663.
- [6] Shms El Din, A.M.,Wang, L, Mechanism of corrosion inhibition by sodium molybdate. *Desalination*,1996,29-43.
- [7] Walfried Plieth, *Electrochemistry for Materials Science*, 2008.
- [8]Zheludkevich,M.L;Serra, R; Montemor, M.F; Yasakau, K.A; Salvado, I.M.M;; Ferreira, M.G.S, Nanostructured sol-gel coatings doped with cerium nitrate as pre-treatments for AA2024-T3:Corrosion protection performance. *Electrochim. Acta*, 2005, 51,208-217
- [9] “Inhibitor Efficiency” <<https://www.corrosion-doctors.org>>

Study on the Condition of Local Chromite Refractory Lining that Used in Induction Furnace

Waing Waing Kay Khaing Oo¹, Shwe Wut Hmon Aye²

Department of Metallurgical Engineering and Materials Science^{1,2}

West Yangon Technological University^{1,2}

Hlaing Thar Yar Township, Yangon Region, Myanmar^{1,2}

waingkaykhine@gmail.com¹, hmon152@gmail.com²

Abstract

Chromite is not only resource for chromium or other chrome –bearing chemicals but also raw materials for refractories. The chromite is one of the neutral refractory based on the chemical compositions. Firstly, the chemical compositions and refractoriness were firstly measured. To study the use of chromite raw material as induction furnace lining, five different sizes of chromite were mixed. Boric acid was used as binder. Cast iron and aluminum alloys were used as materials for melting. The lining was tested for a total of only (14) hours and (4) heat. After each test, the condition of the lining was studied and it was observed that no severe damage or erosion of the lining took place. In this work, the chromite ore from Mwetaung area was used as raw material.

Keywords- Chromite, Refractory lining, Induction furnace.

1. Introduction

Refractories are inorganic, non-metallic and heat resistant materials that can withstand abrasive, corrosive, liquids or gases at high temperatures. The refractory materials are classified on the basis of chemical composition as acid, basic or neutral [7].

Acid refractories are those which are attacked by basic slags. These are not affected by acid slags and hence can be safely used where the environment is acidic. Examples of acid refractories are high silica, quartz and fireclay [1]. Basic refractories are those which are attacked by acid slags. But they do not react with basic slags, these refractories are suitable for furnace lining where the environment is basic. Magnesite and dolomite, chrome-magnesite and magnesite – chrome are basic refractories. Chrome and high alumina are neutral refractories and that are neither attacked by acid nor by basic slags.

Induction furnaces are used for melting cast iron, mild steel various alloy steels in foundries and making of steel in mini steel plants. Refractory lining is the important part of induction furnace. Furnace performance is directly related to the performance of its lining [4].

Normally, the selection of refractory for furnace lining is based on the type of slag generated during melting. Silica lining has good endurance against

thermal shock but poor resistance against steelmaking slags. It corrodes by the chemical interaction when there is basic slag made during steelmaking. Magnesite lining is more compatible chemically but has poor thermal shock resistance and develops vertical cracks during service. Neutral lining has advantage over both silica and basic lining in terms of chemical reaction, thermal shock resistance. For this, neutral lining in induction furnaces are widely used in metallurgical industries. Alumina and Magnesite compounds are also used in the present practice of neutral lining in induction furnace.

In this work, chromite compound was applied as neutral lining. The raw materials were obtained from Mwetaung area, Chin State. Firstly, the chemical compositions were measured to know the content of chromium oxide. The content of Cr₂O₃ must be at least 30% for refractory purposes. Secondly, fusion and softening temperatures were measured because the refractory materials those withstand the high temperature at which it is to be used. After that, the chromite refractory was used as in an induction furnace and condition of the lining was investigated.

The main aim of this work is to study the characteristics and properties of Mwetaung chromite ore whether it can be used as refractory material or not. So, it will be tested as refractory lining and analyzed its behaviors.

2. Experimental Procedure

The necessary procedures for chromite refractory lining were carried out as followings.

2.1. Analysis of Chromite Ore

The wet analysis method was used to determine the chemical composition of Mwetaung Chromite Ore.

2.2. Fusion and Softening Temperatures

To examine fusion and softening temperatures of chromite ore, the Pyrometric Cone Equivalent (PCE) method was used. The seger cones that produced by the Japan Seger Cone Association were used in this testing. The prepared chromite cones mixed with different binders were tested with three seger cone (#35, #36, and #37) for three times. The boric acid, sodium silicate and

magnesium chloride were used as different binders in this testing [6].

2.3. Sample Preparation

In this step, cleaning, washing, drying, grinding and sieving are included.

2.3.1. Cleaning

Various impurities such as dust, insects and soil particles may contain in the raw chromite ore. So, the raw ore was cleaned by wasing with water at least three times and then drying was carried out naturally.

2.3.2. Crushing and Grinding

The original raw size material was in the range between 20 mesh sizes to 1 inch cube. For this experiment, the materials are required for five different sizes. For this, the different milling machines as shown in Figure 1 are used. The gyratory crusher was used to crush 1.5" size to under 0.5" size. The jaw crusher was used to obtain under 5 mesh size to different under size to powder. Powder particles were obtained by using pulverizer.

2.3.3. Screening Analysis

The required sizes of material are

- a) + 8 mesh size
- b) -8 to +28 mesh size
- c) -28 to +65 mesh size
- d) -65 to +150 mesh size
- e) -150 mesh size.

To obtain the above sizes, the crushed and ground particles were screened by using different types of sieve number. The sieve shaker which contains different types of sieves was shown in Figure 2.



(a) Gyratory Crusher



(b) Jaw Crusher



(c) Ball Mill



(d) Pulverizer

Figure 1. Different Types of Milling Machines



Figure 2. Sieve Shaker

2.3.4. Used as Induction Furnace Lining

0.5 ton induction furnace was used to test the lining of local chromite refractory material as shown in Figure 3. The former was made of mild steel sheet and it was 2 mm thickness. It was shown in Figure 4 which was needed for lining preparation. In Figure 5, the dimension of the former is shown. Vent holes which had

about 3mm diameters were made around the former side wall for the escape of moisture.

The weight(kg) and mesh size used for lining preparation are shown in table 1.Boric acid was applied as the binder.The total weight for the lining preparation was 150 kg. The different ratios of chromite materials and boric acid were used in concrete mixer as shown in Figure 6.The mixing time was 1 hr.Firstly, the cooling coil was inspected to check whether the water leakage tool place or not.

The sealing of inductor was also needed to check and the diameter of coil was leveled out with a coil grout.Figure 7 shows the setting up the coil into the furnace . As an insulating layer, the asbestos cloth was placed over the coil as shown in Figure 8.Moreover, asbestos sheet was put over the asbestos clothes as shown in Figure 9.After all of these steps, the inner height of the induction furnace was needed to measure.



Figure 3. Induction Furnace



Figure 4. The Former

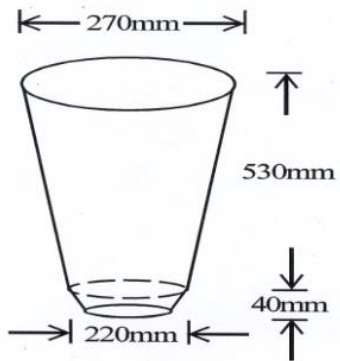


Figure 5. Dimension of the Former

First of all, the bottom of the furnace was rammed. To get the thickness of 120 mm, the mixture was poured into the bottom about 240 mm thick and rammed by using the appropriate rammers and vibrator. And then, the mixture was again filled about 240 mm thick and rammed to get the total thickness of 240 mm.



Figure 6. The Concrete Mixer



Figure 7. Setting up the Coil



Figure 8. Covering by Asbestos Cloth



Figure 9. Covered with Asbestos Sheet



Figure 10. Settlement of the Former

Table 1. Usage of Mesh (size) Number, Percentage and Weight of Chromite and Boric Acid for 0.5 ton Induction Furnace Lining

No	Material	Size	Percent	Weight (kg)
1.	Chromite	+ 8 mesh	11.08	16.62
		-8 to +28 mesh	35.48	53.22
		-28 to +65 mesh	18.73	28
		-65 to +150 mesh	13.06	20
		- 150 mesh	21.65	33
2.	Boric acid		1.5	2.2
	Total			153.04

As shown in Figure 10, the former was firmly seated on the bottom surface in the furnace. Any voids between the former and its base can cause cracks from insufficient support. And so, a substantial weight of scrap was placed into the former to prevent shifting during ramming. The prepared mixture was rammed layer by layer using the same tools for the sidewall. The side by side layer was loosened slightly to avoid lamination. The workers changed their positions alternatively around the former while they were ramming.

The lining was rammed to the level of the topmost turn of the inductor. To avoid excessive shrinkage during curing, the capping material (refractory clay, chromite and silicate) was not excessively wet. After that the lining was dried. When the lining was ready for use, some iron blocks were placed into the former. As the power was switched on, the current appeared in the iron blocks and the heat developed was transferred to the adjacent layer of the lining as shown in Figure 11.

The power should be applied slowly to gently warm up the chamber to avoid cracking of the lining. The preheating temperature cycle was holding at 200°C for 2 hr, keeping between 200°C to 600°C for 3 hr, 600°C to 900°C for 2 hr, 900°C to 1100°C for 2 hr 1100°C to 1350°C for 1hr and temperature 1350°C for keeping time.

The total time was about 10 hr for this process. If the power was applied too rapidly, uneven heating of the former could result in potentially catastrophic failures such as thermal shock and hazardous steam explosions. After preheating, the furnace was charged with some blocks of cast iron and melting operation was started.



Figure 11. Preheating the Furnace



Figure 12. Pouring into the Ladle

After getting that temperature, all the blocks were melted down. Then the molten cast iron was poured into the ladle as shown in Figure 12. From this, the molten cast iron was poured into the mold. After that, the lining was cleaned of remaining metal and slag and the condition of the lining was inspected visually.

3. Results and Discussions

In this test work, the chromite ore obtained from Mwetaung Area is tested as the raw materials. The necessary experiments are carried out. The obtained results are given below and discussed.

3.1. Chemical Compositions

For the use of refractory purposes such as furnace lining, the Mwetaung chromite ore was firstly determined the chemical compositions. The comparison

of test results and typical compositions are shown in table 2 and discussed below.

By comparing these two results, it can be seen that the chemical composition of chromic oxide in Mwetaung chromite ore is within the range of typical compositions and that can gave good refractoriness. For this reason, it can be used as the refractory material.

Table 2. Comparison between Typical and Mwetaung Chromite Ore Compositions

No.		Standard Compositions	Mwetaung Chromite Ore Compositions
1	Chromic Oxide	30 to 50 %	49.98%
2	Iron Oxide	12 to 16%	15.7%
3	Silica	3 to 6 %	4.68%
4	Alumina	13 to 30%	12.14%
5	Magnesia	14 to 20%	15.26%
6	Lime	Up to 1%	ND

3.2. Fusion and Softening Temperatures

Following the Pyrometric Cone Equivalent (PCE) test results, the prepared chromite cones did not soften or fusion up to 1820°C. It can also be seen that the different binders could not affected in refractoriness. For this, the Mwetaung chromite ore has a fusion point of over 1825°C and the three different binders can be used.

3.3. Chromite Refractory Lining Condition

The chromite ore was tested as refractory lining in 0.5ton induction furnace. The lining condition after melting is discussed below. The lining thickness of side wall and bottom were measured before the operation started. The lining thickness of sidewall was 130mm and the bottom was 240 mm, respectively.

3.3.1. First Times Lining Testing by Melting Cast Irons

For the first heat, cast iron was melted. The temperature recorded was 1350°C. The melting time was taken about 4 hrs. After melting, the lining was cleaned of remaining metal and slag and inspected visually. After melting condition, the lining thickness of side wall and bottom were measured again and compared to the original dimensions. By comparing these, it was observed that there was no difference in the lining thickness.

3.3.2. Second and Third Times Lining Testing by Melting Aluminum Alloys

For the second and third heats, aluminum alloys were melted. The temperature recorded was 700°C. The melting time was 30 minutes for each melting. After melting, the lining was cleaned and inspected visually.

The lining condition after third time heating is shown in Figure 13.

3.3.2. Observation the Lining Condition

Although the lining had been used for three melts, no change in the lining thickness was observed. It can be noted that the erosion of the lining had not occurred. But small cracks which were formed at the upper region of the side wall were detected. This was because good sintering condition was not obtained and temperature difference was occurred during melting. The performance of chromite ore is mentioned in table 3.

It can be seen from that the use of Mwetaung chromite ore as a refractory lining had tested for total of only (14) hours and (4) heats _ two for cast iron and two for aluminum alloy. After each test, the condition of the lining was studied and it was observed that no damage or erosion of the lining took place.



Figure 13. Lining Condition after Third Time Melting

Table 3. Performance of Chromite Ore

No.	Melted metal	Time (hr)	Condition of Lining	Remark
1.	Cast Iron	10	-	Preheating time
2.	Cast Iron	4	No Change in lining thickness	Melting
3.	Aluminum alloy	0.5	No change in lining thickness	Melting
4.	Aluminum alloy	0.5	During short time melting, No damage or erosion is formed	Melting
	Total	15		

The number of tests that could be made depended on the restrictions and limitations of the factory such as furnace condition, necessary equipment, cost, time, labors and power supply. Therefore, the obtained results were discussed on the basis of melting on 14 hours of total melting time.

4. Conclusions

In this work, the chromite ore obtained from Mwetaung area was tested as the raw materials. According to the test results. The chemical composition of Mwetaung chromite was within the range of standard

compositions. According to the PCE test results, it does not soften or fused up to 1820°C. Because of limited testing facilities, some experiments could not be carried out.

For testing the lining, fixed size distribution ratio and one type of binder, sodium silicate was used. The other binders such as boric acid and magnesium chloride also should be tested and studied the effect of different binder contents if possible. In this study, locally available metal scraps were charged during melting. If possible, the known chemical analysis of metal should be charged. According to the type of slag produced, the acid or basic melting practice can be chosen. In this tests, chromite refractory lining was tested for a total of only (14) hours and (4) heats. The number of tests that could be made depended on the restrictions and limitations of the factory. If possible, many tests should be carried out. However, various possible attempts were made to test the feasibility of chromite refractory lining.

According to the results obtained from both determination of properties and test works, Mwetaung chromite ore can be accepted as refractory material for induction furnace lining.

5. References

- [1] Alfred B. Searle.1940, Refractory Materials: Their Manufacture and Uses.
- [2] D.Turner.1934, Special Refractories for Metallurgical Research at High Temperatures, Trans. Ceramic Soc., 33.
- [3] Hubble, D.H. 2000, Steel Plant Refractories, The Making, Shaping and Treating of Steel.
- [4] James P.Bennett, Jeffery D Smith, 2006, Fundamentals of Refractory Technology, Volume 125
- [5] Kenich Sakurai. Refractories, Nagoya International Training Center Japan International Cooperation Agency
- [6] MIS Myanmar Ceramic Industries, 2001, Refractories Bricks Manufacturing Plant, Quality Control Manuals.
- [7] Norton, F.H. 1949, *Refractories*, 3rd ed., Mc Graw-Hill Book Company, New York.
- [8] “Refractory Lining of Coreless Induction Furnace” <<https://www.ispatguru.com>>

The Optical Properties of Natural Dye from Spinach Leaves as Sensitizer for Dye-Sensitized Solar Cells

Nan Kyi Kyi Thein¹, Thwe Thwe Aye², Aung Htet³

Materials Science Research Laboratory, Department of Physics^{1,2,3}

University of Mandalay^{1,2,3}

nancykyithein@gmail.com¹, thwethweaye.mdy2019@gmail.com², aunghtet7694@gmail.com³,

Abstract

Spinacia oleracea, well known as spinach leaves, were used as sensitizers for Dye-sensitized solar cell (DSSC). The optical properties such as the optical absorbance and band gap energy value of the obtained spinach dye solutions with different concentrations, solvents (ethanol, acetone, isopropanol (IPA) and distilled water) and temperatures were studied using UV-vis spectrophotometer in the range of (300-800) nm. From this work, the optimal concentration is 180×10^3 ppm. In spinach dyes, there are two peaks. The characteristic of the first peak is 435 nm and the second peak is 665 nm. They are attributable to the mixtures of chlorophyll a and b. The absorption peak intensity is the highest in acetone at 60 °C. The band gap of the dye is also presented by extracting the chlorophyll in acetone which is 2.89 eV and the absorption coefficient of 2.52 km⁻¹ at the wavelength of 430 nm.

Keywords: Red Spinach dye, Photosensitizer, Absorbance and Band gap energy

1. Introduction

Dye-sensitized solar cell (DSSC) is a low-cost solar cell belonging to the group of thin film solar cells. It is based on a semiconductor formed between a photo-sensitized anode and an electrolyte, a photoelectrochemical system. Dye-sensitized solar cells were first proposed by Gratzel (1991). A DSSC is the third generation photovoltaic device for low cost conversion of solar energy into electrical energy [1]. Previously, DSSC employs ruthenium (II) polypyridinic complex as a sensitizer of wide-band gap semiconductor but due to costly and complicated in sensitizing the complexes also containing heavy metal and producing environmental polluting, another method is replacing it using natural dyes from fruits, plants and leaves, which offered cost efficiency, non-toxicity and complete biodegradation. Natural dyes play a key role in harvesting sunlight and transferring solar energy into electrical energy [2-3]. The advantages of natural dyes include their low cost and availability [4].

Some fruits, plants, flowers and leaves displayed various colors and contained several pigments, which can be simply extracted and then used as sensitizer because most of green plants contained a lot of

chlorophyll, which help in absorbing photon from sunlight [5]. Chlorophyll can absorb light from red, blue and violet wavelengths and obtains its color by reflecting the green wavelength. The strong absorption peaks in the visible region located at 420 nm and 660 nm wavelengths that can be used as a natural sensitizer in the visible light range [6].

In this work, natural dyes were extracted from spinach leaves used as a sensitizer in DSSC. The influence of different extracts solvent from ethanol, IPA, acetone and distilled water to extract the chlorophyll pigments from spinach. These extracted dyes were characterized by UV-Vis absorption spectrometer. Spinach leaves have been investigated from its absorption spectrum, band gap and also absorption coefficient.

2. Experiment

This experimental section describes the synthesis and characterization of spinach dye solution.

2.1 Preparation of Spinach Dye Solution

The collected fresh spinach leaves was washed multiple times with water to remove all the impurities and contamination. The cleaned spinach leaves were ground using motor and pestle to make spinach paste. This paste was weighed 0.3g and then it was placed in glass bottle. 5 ml of ethanol was added in glass bottle and stirred with magnetic stirrer at different temperatures (25°C, 45°C, 60°C, 75°C, 90°C and 110°C) for 30 minutes at 400rpm. As well as, 5ml of different solutions such as (acetone, isopropanol and distilled water) was added in each glass bottle at different temperatures for 30 minutes. The resulting liquid was filtered out using filter paper and then dye was extracted. The absorption spectra of these dyes have been investigated by UV-vis spectrophotometry. The extraction of spinach dye solution is shown in Figure 1.

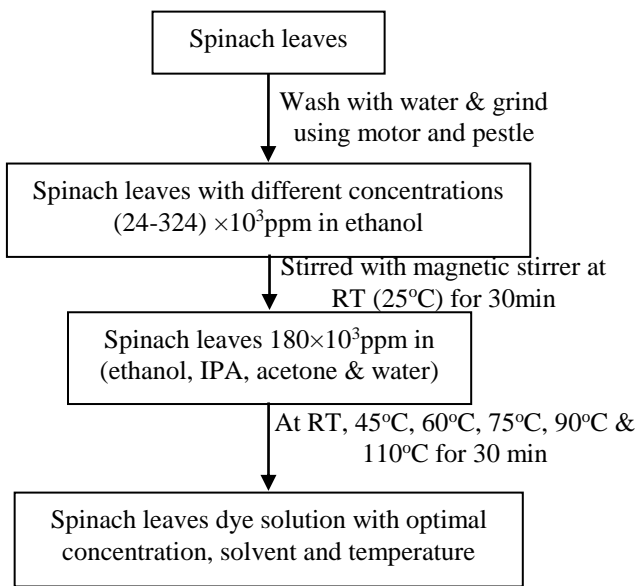


Figure 1. Flow Chart for Synthesis of Spinach Dye Solution

2.2 Characterization

In this work, UV-vis spectrophotometry was used as characterization for spinach dye solution.

2.2.1 UV-vis Spectrophotometry

UV-vis spectrophotometry is a technique to measure absorbance and wavelength of the samples not only in the visible region but also in the UV region. The optical properties of spinach dye solution were explored by UV-vis spectrophotometer (GENESYS 10S). The absorption spectra of spinach dye solutions were recorded in the wavelengths ranging from 300nm to 800nm. A reference solution was used as baseline scan before the measurement.

3. Results and Discussion

3.1 Optical Absorption of Spinach Dye Extracts

3.1.1 Effect of Concentration

Firstly, we have studied the effect of concentration on optical absorption of dye extracted from spinach leaves. Figure 2 shows the optical absorption spectra of spinach dye extracts in different concentrations (24-324) × 10³ ppm in ethanol. The peak intensities increased with increasing dye concentration. The optimal concentration was obtained at 180×10³ ppm. In this figure, two peaks were found; the characteristic of the first peak is 435nm and the second peak is 665nm; they are attributable to the mixture of chlorophyll a and b. The peak positions of spinach dye solutions being studied remained unchanged. Beyond the optimal

concentration of 180×10³ ppm at 435nm, the peak intensities were overlap and complicated.

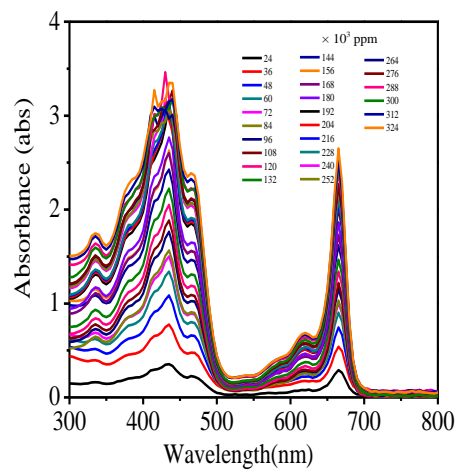


Figure 2. The Optical Absorption Spectra of Spinach Dye Extracts at Different Concentrations in Ethanol.

3.1.2 Effect of Solvent

Secondly, we have studied the effect of solvent on optical absorption of dye extracted from spinach leaves. Figure 3 depicts the optical absorption spectra of spinach dye extracts in ethanol, acetone, IPA and distilled water in the spectra range of (300-800) nm at different temperatures. Both extracts exhibited two prominent absorption peaks (λ_{max}); ~ 435nm and ~ 665nm. The λ_{max} of 425 nm and 660 nm are the characteristics peak maximum for the absorption of chlorophyll [6-7]. The maximum wavelength (λ_{max}) of spinach leave extracts was almost invariant in four different solvents at different temperatures (45 °C, 60 °C and 75 °C) except for room temperature RT (25 °C) and 90 °C. However, the absorption peak intensity of spinach dye extracts was higher in acetone than in the other. It is expected that the concentration of dye extracts would be higher in acetone than in the other solvents at different temperatures, probably because of higher solubility. Modulation of absorption peak intensities can be related to different degrees of solubility in different solvents. Thus for a particular extract, it is crucial to select a proper solvent for dye solubility to maximize the absorption intensity.

3.1.3 Effect of Extracting Temperature

Following the effect of concentration and solvent, the effect of extracting temperature on the optical absorption of spinach dye extracts was also studied. Figure 4 (a) shows the optical absorption spectra of spinach leaves extract at different temperatures (25 °C, 45 °C, 60 °C, 75 °C and 90 °C) in ethanol. The highest absorption intensity was obtained at 25 °C in ethanol. When the extracting temperature was raised from 25°C to 90 °C, absorption intensity decreased. This may be

due to the distortion of spinach dye structure at 90 °C. In ethanol, the peak positions were invariant at different temperatures (25°C, 45 °C, 60 °C and 75 °C). The peak position becomes red shift at 90°C. Figure 4 (b) shows the optical absorption spectra of spinach leaves extract at different temperature (25°C, 45 °C, 60 °C and 75 °C) in acetone. The highest absorption intensity was obtained at 45 °C in acetone.

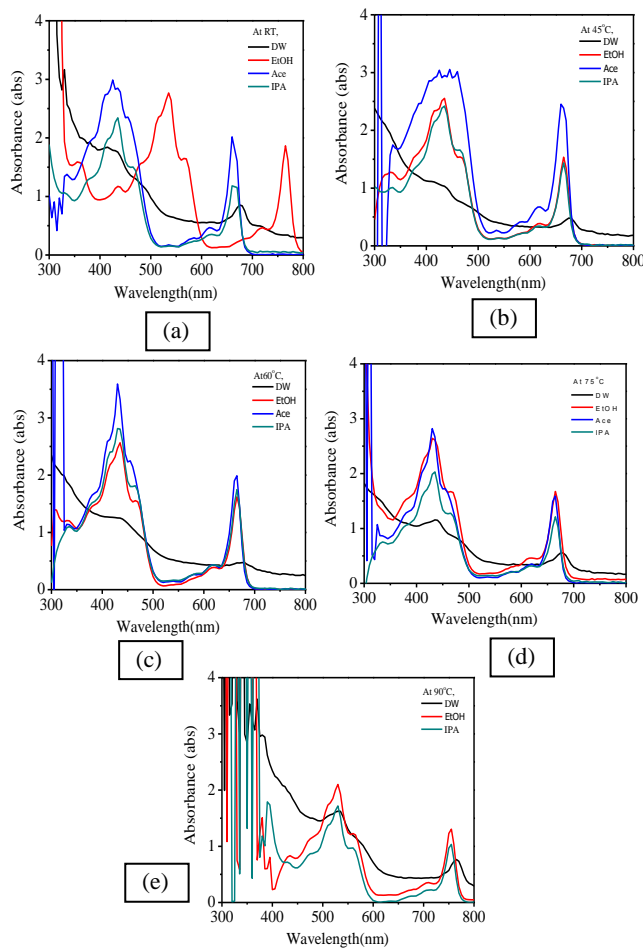


Figure 3. The Optical Absorption Spectra of Spinach Dye Extracts in Ethanol, Acetone, IPA and Distilled Water at Different Temperatures.

The absorption intensity was decreased at different temperatures (25°C, 60 °C and 75 °C) than 45 °C. In acetone, the λ_{\max} was invariant at different temperatures (25°C, 45 °C, 60 °C and 75 °C). Figure 4 (c) shows the optical absorption spectra of spinach leaves extract at different temperatures (25°C, 45 °C, 60 °C, 75 °C and 90 °C) in IPA. The highest absorption intensity was obtained at 60 °C in IPA. The absorption intensity was decreased at different temperatures (25 °C, 45 °C, 75 °C and 90 °C) rather than 60 °C. In IPA, the peak positions were invariant at different temperatures (25°C, 45°C, 60 °C and 75 °C). The peak position has become red shift at 90 °C. Figure 4 (d) shows the optical absorption spectra of spinach leaves extract at different temperatures (25°C, 45 °C, 60 °C, 75 °C, 90 °C and 110

°C) in distilled water. The highest absorption intensity was obtained at 110 °C in distilled water. The absorption intensity was decreased at different temperatures (25°C, 45 °C, 60 °C, 75 °C and 90 °C) rather than 110 °C. The peak position was changed at different temperatures. From this study, it is found that for all extracts being studied, the maximum absorption peak positions (λ_{\max}) varies in four different solvents (ethanol, acetone, IPA and distilled water) at different temperatures, however, the absorption peak intensity of spinach dye in acetone is highest in other solvents at different temperatures.

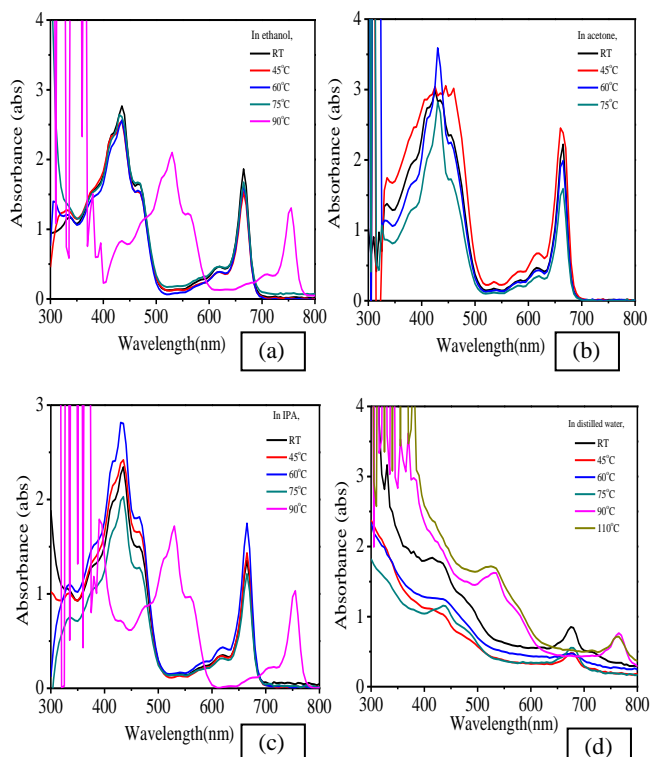


Figure 4. The Optical Absorption Spectra of Spinach Leaves Extract at Different Temperatures in (a) Ethanol (b) Acetone (c) Isopropanol and (d) Distilled Water.

3.2 Band Gap Energy of Spinach Dye Solutions (Method 1)

The value of band gap energy (E_g) of spinach dye solutions was analyzed by using plotted for direct transition $(\alpha h\nu)^2$ versus $h\nu$ of the sample. The band gap energy of the samples was determined by using the following formula;

$$(\alpha h\nu) = A (h\nu - E_g)^n \quad (1)$$

Where, α = absorption coefficient
 $h\nu$ = the energy of photon
 E_g = the direct band gap
 A = the constant

The exponent ‘n’ depends on the type of transition. For direct allowed transition n=1/2, for indirect allowed transition n=2 and for direct forbidden transition n=3/2.

The $(\alpha h\nu)^2$ vs $h\nu$ plot of spinach dye solutions was shown in Figure 5. The extra plotting linear region gives the values of band gap (E_g) of spinach dye solution. Moreover, the band gap energy of spinach dye solutions was listed in Table 1. From these results, it was observed that the values of band gap are 2.49eV at 25°C, 45°C, 60°C and 75°C, and 2.08eV at 90°C in ethanol. The band gap values in acetone were 2.48eV, 2.45eV, 2.48 eV, 2.52eV at 25°C, 45°C, 60°C and 75°C respectively. Moreover, the band gaps of dye in isopropanol were 2.50eV at 25°C, 45°C, 60°C and 75°C, and 2.1eV at 90°C. And then, the band gap values became 2.28eV, 2.30eV, 2.30eV, 2.50eV and 1.95eV at 25°C, 45°C, 60°C, 75°C, 90°C and 110°C respectively in distilled water.

Table 1. The Band Gap Energy of Spinach Dye Solutions in Different Solvents at Different Temperatures

Dyes	Extract solvent	Extract Temperature	Bandgap (eV)
Spinach	Ethanol	RT(25 °C)	2.49
		45 °C	2.49
		60 °C	2.48
		75 °C	2.49
		90 °C	2.08
	Acetone	RT(25 °C)	2.48
		45 °C	2.45
		60 °C	2.48
		75 °C	2.52
	Isopropanol	RT(25 °C)	2.50
		45 °C	2.49
		60 °C	2.50
		75 °C	2.49
		90 °C	2.10
	Distilled water	RT(25 °C)	2.28
		45 °C	2.30
		60 °C	2.30
		75 °C	2.50
		90 °C	1.95
		110 °C	1.95

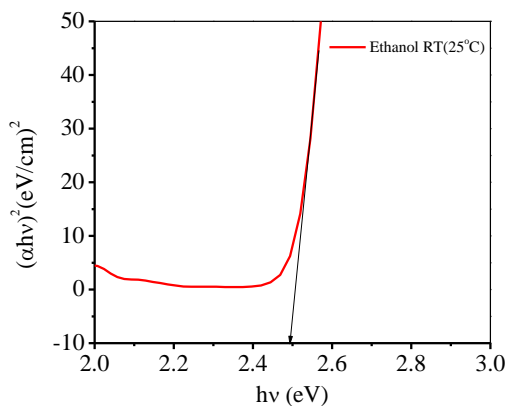


Figure 5. Plot of $(\alpha h\nu)^2$ Vs $h\nu$ for Spinach Dye Solutions in Ethanol at 25 °C.

3.3 Band Gap Energy and Absorption Coefficient of Spinach Dye Solutions (Method 2)

The band gap energy and absorption coefficient of natural dye solutions was listed in Table 2. The energy of the band gaps (E_g) of these samples at different temperatures were calculated by using the formula (1). From this result, it was observed that the value of band gap for ethanol is 2.86eV at 435nm for 25°C, 45°C and 60°C as well as the value of the band gap energy were 2.89eV and 2.34eV at 75°C and 90°C respectively. In acetone, the band values are 2.92eV at 25°C, 2.79eV at 45°C, 2.89eV at 60°C and 2.89eV at 75°C respectively. Moreover, in isopropanol, the band gap values are 2.86eV at 25°C, 2.86eV at 45°C, 2.89eV at 60°C, 2.83eV at 75°C. and 2.32eV at 90°C respectively. For distilled water, the energy values are 3.00eV, 2.93eV, 2.35eV, 2.32eV and 2.37eV at 25°C, 45°C, 60°C, 75°C, 90°C and 110°C respectively.

From this result, the optimal concentration is 180×10^3 ppm. In ethanol, the value of band gap is 2.86 eV, 2.86 eV, 2.86 eV and the absorption coefficient is 2.49 km^{-1} , 2.49 km^{-1} , 2.49 km^{-1} at 435 nm for 25°C, 45 °C and 60 °C respectively. At 75 °C, the value of band gap is 2.89 eV and the absorption coefficient is 2.52 km^{-1} at 430 nm. The value of band gap is 2.34 eV and the absorption coefficient is 2.04 km^{-1} at 530 nm for 90 °C. As temperature increases, the absorption edge wavelength becomes red shift at 90°C.

In acetone, the value of band gap is 2.92 eV and the absorption coefficient is 2.55 km^{-1} at 425 nm for 25°C. At 45 °C, the value of band gap is 2.79 eV and the absorption coefficient is 2.43 km^{-1} at 445 nm.

The value of the band gap is 2.89 eV, 2.89 eV and the absorption coefficient is 2.52 km^{-1} , 2.52 km^{-1} at 430 nm for 60 °C and 75 °C respectively as well. The maximum peak intensity is 430 nm at 60 °C in acetone.

In isopropanol, the value of band gap is 2.86 eV and the absorption coefficient is 2.49 km^{-1} at 435 nm for 25°C and 45°C. For 60°C, the value of band gap is 2.89 eV and the absorption coefficient is 2.52 km^{-1} at 430

nm. The value of band gap is 2.83 eV and the absorption coefficient is 2.46 km^{-1} at 440 nm for 75 °C. For 90 °C, the band gap is 2.32 eV and the absorption coefficient is 2.02 km^{-1} at 535 nm. As temperature increases, the absorption edge wavelength becomes red shift at 90 °C.. In distilled water, the values of band gap are 3 eV, 2.93 eV, 2.86 eV, 2.35 eV, 2.32 eV and 2.37 eV and the absorption coefficient are 2.61 km^{-1} , 2.55 km^{-1} , 2.45 km^{-1} , 2.04 km^{-1} , 2.02 km^{-1} and 2.06 km^{-1} for 25 °C, 45 °C, 60 °C, 75 °C, 90 °C and 110°C respectively. The absorption edge wavelength becomes red shift at different temperatures because the peak intensity shifted towards the red part of the spectrum.

4. Summary and Conclusion

The natural dyes were extracted from spinach leaves as a sensitizer for dye-sensitized solar cells. In spinach dye, two peaks were found; the characteristic of the first peak is 435 nm and the second peak is 665 nm. They are attributable to the mixture of chlorophyll a and b. The natural dyes showed sharp absorption peaks in the visible region, (400-700) nm. The optical properties such as the optical absorbance and band gap energy of the obtained spinach dye solutions were studied against different concentrations, solvents and extracting temperatures.

The low absorption intensity is obtained at high extracting temperature in ethanol, acetone, isopropanol and distilled water. The long peak absorbance wavelength, low energy band gap and low absorption coefficient are obtained in ethanol, acetone, isopropanol and distilled water at different temperatures .Therefore, the optical properties of Spinach is a good absorber for dye-sensitized solar cells.

5. Acknowledgement

We are deeply grateful to Professor Dr. Lei Lei Win, Head of Department of Physics, University of Mandalay, for her kind permission to carry out this research work.

Table 2. The Peak Absorbance Wavelength, Absorption Coefficient Range, Band Gap Energy and Absorption Coefficient of Spinach Dye Solutions.

Dye	Extractant	Extract temperature	Maximum Peak Absorbance Wavelength (nm)	Absorption range (nm)	Band gap (eV)	Absorption coefficient (α) Km $^{-1}$
Spinach	Ethanol	RT(25 °C)	435	350-510	2.86	2.49
		45 °C	435	350-510	2.86	2.49
		60 °C	435	350-510	2.86	2.49
		75 °C	430	350-520	2.89	2.52
		90 °C	530	405-610	2.34	2.04
	Acetone	RT(25 °C)	425	350-520	2.92	2.55
		45 °C	445	345-520	2.79	2.43
		60 °C	430	345-515	2.89	2.52
		75 °C	430	350-520	2.89	2.52
	Isopropanol	RT(25 °C)	435	350-520	2.86	2.49
		45 °C	435	350-520	2.86	2.49
		60 °C	430	350-520	2.89	2.52
		75 °C	440	355-520	2.83	2.46
		90 °C	535	455-610	2.32	2.02
	Distilled water	RT(25 °C)	415	395-535	3.00	2.61
		45 °C	425	395-530	2.93	2.55
		60 °C	435	415-525	2.86	2.45
		75 °C	435	415-530	2.35	2.04
		90 °C	535	495-630	2.32	2.02
		110 °C	525	495-620	2.37	2.06

6. References

- [1] H. Chen, et al., “Dye-sensitized solar cells combining ZnO nano-tip arrays and non-liquid gel electrolytes”, Miner. Met. Miner. Soc., J.Electron.Mater, **38** (2009)1612-1617.
- [2] A.S Polo, et al., “Blue sensitizers for solar cells: Natural dyes from Clafate and Jaboticaba”, J.Sol. Energy Mater. Sol. Cells, **90** (2006) 1936-1944.
- [3] M.S. Abdel-Latif, et al., “Plant Seeds-Based Dye-Sensitized Solar Cells”, J. Mater. Sci. Appl, **4** (2013) 516-520.
- [4] J. Wu, et al., “Solar Energy”, **80** (2006) No 6, 209.
- [5] N.T.R.N. Kumara, et al.,“Layered co-sensitization for enhancement of conversion efficiency of natural dye sensitized solar cells”, J. Alloys Compd, **581**(2013) 186-191.
- [6] A.B. MohamadKadhum, et al., “Effect of solvents on the extraction of natural pigments and adsorption onto TiO₂ for dye-sensitized solar cell applications”, J. Spectrochim. Acta, Part A: Mol. Biomol. Spectrosc., **138** (2015) 130-137.
- [7] N.K.K. Thein, et al., “Red Spinach Dye Extracts as Photosensitizer in Solid State Dye-Sensitized Solar Cells: Varying Relative Ratio of Co-solvents and Dye Extracting Temperature”, Journal of Myanmar Academy of Arts and Science, **14** (2015) 155-162.